

## REPORT DOCUMENTATION PAGE

Form Approved  
OMB No. 0704-0188

The public reporting burden for this collection of information is estimated to average 1 hour per response, including the time for reviewing instructions, searching existing data sources, gathering and maintaining the data needed, and completing and reviewing the collection of information. Send comments regarding this burden estimate or any other aspect of this collection of information, including suggestions for reducing the burden, to the Department of Defense, Executive Services and Communications Directorate (0704-0188). Respondents should be aware that notwithstanding any other provision of law, no person shall be subject to any penalty for failing to comply with a collection of information if it does not display a currently valid OMB control number.

PLEASE DO NOT RETURN YOUR FORM TO THE ABOVE ORGANIZATION.

1. REPORT DATE (DD-MM-YYYY) 31-08-2010	2. REPORT TYPE Final Technical Report (2 volumes)	3. DATES COVERED (From - To) Jun 2005 - Aug. 2010		
4. TITLE AND SUBTITLE  "Basic Research Investigations into Multimode Laser and EM Launchers for Affordable, Rapid Access to Space" (Volumes 1 and 2)		5a. CONTRACT NUMBER FA9550-05-1-0392		
		5b. GRANT NUMBER FA9550-05-1-0392		
		5c. PROGRAM ELEMENT NUMBER		
6. AUTHOR(S)  Myrabo, Leik N., Salvador, Israel I., and Kenoyer, David A.		5d. PROJECT NUMBER		
		5e. TASK NUMBER		
		5f. WORK UNIT NUMBER		
7. PERFORMING ORGANIZATION NAME(S) AND ADDRESS(ES)  Rensselaer Polytechnic Institute Mechanical, Aerospace, and Nuclear Engineering Department 110- Eighth Street, Troy, NY 12180-3590		8. PERFORMING ORGANIZATION REPORT NUMBER  RPI-TR-A11602/ TR-A11848		
9. SPONSORING/MONITORING AGENCY NAME(S) AND ADDRESS(ES)  Air Force Office of Scientific Research (AFOSR) Arlington, VA 22203		10. SPONSOR/MONITOR'S ACRONYM(S)  AFOSR		
		11. SPONSOR/MONITOR'S REPORT NUMBER(S)  FA9550-05-1-0392		
12. DISTRIBUTION/AVAILABILITY STATEMENT  Unclassified. Distribution Unlimited		AFRL-AFOSR-VA-TR-2016-0656		
13. SUPPLEMENTARY NOTES  None				
14. ABSTRACT  This basic research effort on pulsed airbreathing/rocket laser propulsion, investigates the physics of laser energy deposition into stationary and hypersonic working fluids, inclusive of electrical breakdown, ignition of laser-supported detonation waves (LSD), and blast wave propagation over thruster impulse-generating surfaces. The future application of AFOSR interest for this basic research endeavor is the laser launch of nano- and micro-satellites (i.e., 1-100 kg payloads) into Low Earth Orbit (LEO), at low cost and "on-demand." The present dual-pronged, combined experimental/numerical research campaigns centered on both static and hypersonic experiments with representative 2D and 3D laser-thruster geometries, using the Lumenics TEA-622 (~200J, ~100ns) and K922M (20-40J, ~100ns) CO2 lasers. Laser scramjet experiments were performed in the T3 tunnel at the Henry T. Nagamatsu Laboratory of Aerothermodynamics and Hypersonics (HTNLAH). Time-dependent surface pressure distributions were measured over thrust-generating surfaces following laser energy deposition; delivered impulse and momentum coupling coefficients (Cm) were obtained; Schlieren movies of the impulse generation process were recorded with a high-speed Cordin digital camera, to study the laser breakdown/ blast wave expansion process, and evolving flow field structures in both stationary and hypersonic flow. Time-resolved visualizations of inlet and absorption chamber flowfields, enabled qualitative analysis of dominant phenomena impacting laser-propulsion physics.				
15. SUBJECT TERMS  Laser propulsion; beamed energy propulsion; advanced propulsion; laser/gas interaction; laser-induced breakdown; laser physics; airbreathing and rocket propulsion; lasers; lightcraft.				
16. SECURITY CLASSIFICATION OF:  a. REPORT U b. ABSTRACT U c. THIS PAGE U		17. LIMITATION OF ABSTRACT UU	18. NUMBER OF PAGES	19a. NAME OF RESPONSIBLE PERSON Prof. Leik N. Myrabo
				19b. TELEPHONE NUMBER (Include area code) 802-989-2874

Reset

Standard Form 298 (Rev. 8/98)  
Prescribed by ANSI Std. Z39-18

**- FINAL REPORT -**

**- PART 1 -**

***Volume 1: Static and Hypersonic Experimental Analysis of Impulse  
Generation in Air-Breathing Laser-Thermal Propulsion***

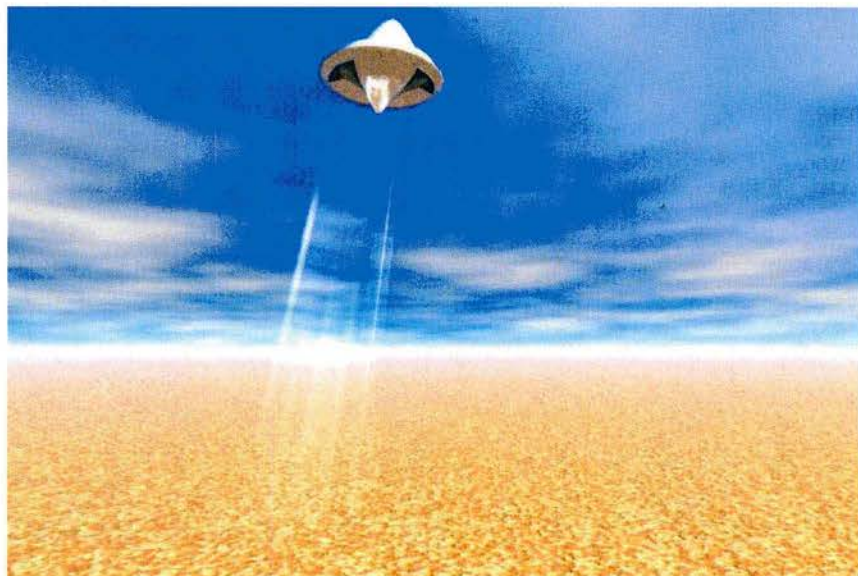
**MURI 05 Grant Title:** "Basic Research Investigations into Multimode Laser and EM Launchers for Affordable, Rapid Access to Space"

**Principal Investigator:** Professor Leik N. Myrabo  
Rensselaer Polytechnic Institute,  
110 8th Street, Troy, NY 12180-3590

**Major Contributors:** Drs. Israel I. Salvador and David A. Kenoyer

**AFOSR Award:** FA9550-05-1-0392

**Research Period:** June 1, 2005 through August 31, 2010 (5 year grant)



Prepared for

**Dr. Mitat Birkan**

**Air Force Office of Scientific Research (AFOSR)  
Arlington, VA 22203**

**31 August 2010**

## CONTENTS

CONTENTS.....	ii
LIST OF TABLES .....	v
LIST OF FIGURES.....	vi
ACKNOWLEDGMENTS .....	<b>Error! Bookmark not defined.</b>
ABSTRACT.....	xiii
1. Introduction.....	1
1.1 Worldwide State-of-the-Art on Beamed Energy Propulsion.....	4
1.1.1 United States.....	6
1.1.2 Europe .....	10
1.1.3 Japan .....	12
1.1.4 Russia .....	15
1.1.5 Brazil.....	17
1.1.6 China .....	18
1.2 Motivation and Objectives.....	18
1.3 Thesis Outline .....	22
2. Laser Induced Breakdown and Impulse Generation Process.....	24
2.1 Early Stage – Cascade Ionization and Plasma Formation .....	24
2.1.1 Metal Surface Air-Breakdown .....	26
2.2 Post-Breakdown Phenomena and Absorption Waves .....	28
2.3 Analytical Model of Surface Pressure History and Impulse Generation .....	35
3. Experimental Apparatus and Procedure .....	40
3.1 Hypersonic Shock Tunnel.....	40
3.2 Lumonics TEA-620 Laser and Beam Propagation .....	44
3.2.1 Laser Beam Diagnostics and Calibration.....	50
3.3 2-D Cross Section Lightcraft Model .....	52
3.4 General Instrumentation .....	56

3.5	Schlieren Visualization Setup .....	57
3.6	Data Acquisition.....	59
4.	Static Experiments .....	<b>Error! Bookmark not defined.</b>
4.1	Surface Pressure Distribution .....	<b>Error! Bookmark not defined.</b>
4.2	Blast Wave Schlieren Visualization .....	<b>Error! Bookmark not defined.</b>
4.3	Impulse Generation Analysis from Surface Pressure Distribution .....	<b>Error! Bookmark not defined.</b>
5	Hypersonic Experiments .....	<b>Error! Bookmark not defined.</b>
5.1	Hypersonic Test Conditions.....	<b>Error! Bookmark not defined.</b>
5.2	Hypersonic Campaign Results for 2D Model...	<b>Error! Bookmark not defined.</b>
5.2.1	Runs 1 to 4 – Initial Runs.....	<b>Error! Bookmark not defined.</b>
5.2.2	Runs 5 to 11 – Troubleshooting Runs...	<b>Error! Bookmark not defined.</b>
5.2.3	Runs 12 to 15 – Shroud Removed .....	<b>Error! Bookmark not defined.</b>
5.2.4	Runs 16 to 19 – Mid-channel Breakdown	<b>Error! Bookmark not defined.</b>
5.2.5	Runs 20 to 24 – Surface Breakdown ....	<b>Error! Bookmark not defined.</b>
5.3	Discussion of the Results.....	<b>Error! Bookmark not defined.</b>
6	Conclusions and Future Work.....	<b>Error! Bookmark not defined.</b>
6.1	Conclusions.....	<b>Error! Bookmark not defined.</b>
6.1.1	Static Experiments .....	<b>Error! Bookmark not defined.</b>
6.1.2	Hypersonic Experiments .....	<b>Error! Bookmark not defined.</b>
6.2	Future Experimental Work .....	<b>Error! Bookmark not defined.</b>
6.2.1	Phase II Hypersonic Campaign with 2D Model	<b>Error! Bookmark not defined.</b>
6.2.2	2 <sup>nd</sup> Generation Two-Dimensional Model	<b>Error! Bookmark not defined.</b>
6.2.3	Axi-symmetric Hypersonic Lightcraft Model	<b>Error! Bookmark not defined.</b>
6.2.4	Airbreathing Laser-Electromagnetic Propulsion	<b>Error! Bookmark not defined.</b>

References.....	<b>Error! Bookmark not defined.</b>
Appendix A – Sensors and Calibration .....	<b>Error! Bookmark not defined.</b>
Appendix B – USA/Brazil BEP Collaboration.....	<b>Error! Bookmark not defined.</b>
Appendix C – Hypersonic Shock Tunnels.....	<b>Error! Bookmark not defined.</b>
C.1 Requirements for Hypersonic Testing .....	<b>Error! Bookmark not defined.</b>
C.2 General Characteristics of a Hypersonic Shock Tunnel	<b>Error! Bookmark not defined.</b>
C.3 Modeling of Shock Tunnel Flow .....	<b>Error! Bookmark not defined.</b>
C.3.1 Thermodynamic Equilibrium Shock Tube Problem	<b>Error! Bookmark not defined.</b>
C.3.2 Nozzle Flow Expansion .....	<b>Error! Bookmark not defined.</b>
Appendix D – Dedicated Laboratory Setup for CO <sub>2</sub> TEA Laser Propulsion Experiments .....	<b>Error! Bookmark not defined.</b>
D.1 Research Vision and Laboratory Strategy .....	<b>Error! Bookmark not defined.</b>
D.2 Laboratory Equipment and Facilities .....	<b>Error! Bookmark not defined.</b>
D.3 Basic Research Program.....	<b>Error! Bookmark not defined.</b>
D.3.1 Current Research .....	<b>Error! Bookmark not defined.</b>
D.3.2 Future Research .....	<b>Error! Bookmark not defined.</b>
D.4 Summary.....	<b>Error! Bookmark not defined.</b>

## LIST OF TABLES

Table 2.1: Laser-supported absorption wave propagation modes (10.6 $\mu\text{m}$ radiation).....	31
Table 3.1: Basic operating conditions of Lumonics TEA 620 laser (stable resonator mode). .....	45
Table 3.2: Lumonics TEA-620 laser pulse characteristics with high gain gas mixture. ....	46
Table 3.3: Pressure sensor inventory and radial distance from laser focal line at the shroud's undersurface. ....	55
Table 4.1: Static (quiescent flow) test run conditions. ....	<b>Error! Bookmark not defined.</b>
Table 4.2: Sensor longitudinal inclination $\Theta$ , and impulse adjustment factor $\sin (\Theta)$ . ....	<b>Error! Bookmark not defined.</b>
Table 4.3: Limits of integration for laser-generated impulse calculations. ....	<b>Error! Bookmark not defined.</b>
Table 4.4: Longitudinal Impulse for sample runs #1, #7, #11 and #12.	<b>Error! Bookmark not defined.</b>
Table 5.1: T3 HST initial conditions and reservoir stagnation conditions achieved during experimental campaign. ....	<b>Error! Bookmark not defined.</b>
Table 5.2: Free stream conditions obtained during experiments, calculated with STCALC (code assumes chemical and thermodynamic equilibrium). ....	<b>Error! Bookmark not defined.</b>
Table 5.3: Model centerbody and shroud inclinations, focal line location, and laser pulse energy for all hypersonic runs. ....	<b>Error! Bookmark not defined.</b>
Table A.1: 2-D Lightcraft sensor models, calibration and ports.	<b>Error! Bookmark not defined.</b>
Table A.2: T3 HST 2-D Lightcraft sensor models, calibration and ports. ....	<b>Error! Bookmark not defined.</b>
Table B.1: Division of responsibilities between RPI and IEAv-CTA in the present campaign. ....	<b>Error! Bookmark not defined.</b>
Table D.1: Single K922M laser operating conditions. ....	<b>Error! Bookmark not defined.</b>

## LIST OF FIGURES

Figure 1.1 Future application for BEP: worldwide transportation. Left: LightPort serviced by space-based power-beaming station. Right: Lightcraft vehicle on launch pad. Palm et al. (2009) .....	4
Figure 1.2 Type 200 Laser Lightcraft in nighttime WSMR free-flight (right); Type 100 Lightcraft with expanding luminous air-plasma exhaust (left). ( <i>Photos by James Shryne III—Courtesy of NASA</i> ) .....	7
Figure 1.3 Cutaway view of German “bell” engine, with ignition pin. Schall and Eckel (2003) .....	11
Figure 1.4 Hypersonic (M=5.0) CFD simulations of a 16 cm diameter Lightcraft flying at 20 km altitude. (Komurasaki et al., 2003) .....	14
Figure 1.5 Microwave-powered Lightcraft (Nakagawa et al., 2003) .....	14
Figure 1.6 LITA concept, upstream beam operation (Komurasaki, 2002) .....	15
Figure 1.7 LITA features in a pusher beam configuration (Sasoh, 2004) .....	15
Figure 1.8 The ALSPE concept vehicle (Rezunkov et al., 2005) .....	16
Figure 1.9 Laser-induced DEAS hypersonic experiments in Brazil. (Salvador, 2008) ...	17
Figure 2.1: Breakdown threshold dependence on incident radiation for Al at 10.6 $\mu$ m, and characteristics times for breakdown initiation. Weyl et al. (1980) .....	28
Figure 2.2: Absorption wave zones of a laser supported plasma from a metallic surface. (Root, 1989) .....	30
Figure 2.3: One-dimensional propagating plasma regions following laser absorption waves. (Root, 1989) .....	32
Figure 2.4: Absorption regions of the one-dimensional waves. (Root, 1989) .....	32
Figure 2.5: Cylindrical blast wave expansion models. Left: vertical oriented axis; Right: horizontal oriented axis (following laser-induced surface breakdown) .....	37
Figure 2.6: Surface pressure vs. time evolution, showing characteristic times. (Pirri, 1973) .....	38
Figure 3.1: T3 Hypersonic Shock Tunnel at the HTN-Laboratory of Aerothermodynamics and Hypersonics. ....	41
Figure 3.2: Hollow HST sting with IR window and mount installed. ....	43
Figure 3.3: ‘Petal catcher’ (left), and stainless steel diaphragms (right) .....	44

Figure 3.4: TEA 620 Laser configuration with unstable resonator cavity. ....	47
Figure 3.5: TEA 622 laser system with Faraday cage (left), and beam footprint (right). ....	48
Figure 3.6: Laser beam transmission path through the laboratory to the test section. ....	50
Figure 3.7: Beam diagnostics table for analyzing laser beam energy and pulse profile. ....	50
Figure 3.8: Beam-splitter energy calibration curve for NaCl sting-window. ....	51
Figure 3.9: Laser pulse profile and integrated pulse energy sampled at NaCl sting- window.....	52
Figure 3.10: Pressure sensor positions within 2D model geometry. ....	53
Figure 3.11: 2-D laser propulsion model installed in T3 hypersonic shock tunnel. ....	54
Figure 3.12: Sensor disposition on shroud undersurface and line focus position used during the static experiments.....	56
Figure 3.13: Schlieren visualization and Cordin camera system setup for T3 test section. .....	58
Figure 3.14: T3 Hypersonic Shock Tunnel showing Schlieren light path and Cordin 550 camera. ....	59
Figure 4.1: Regions for impulse-generation analysis: 1) Inlet compression ramp surface (ignored for static runs); 2) Shroud undersurface; and, 3) Primary Optics (rear parabolic mirror surface).....	<b>Error! Bookmark not defined.</b>
Figure 4.2: Run #12—Pressure distribution over compression ramp. ( $P_{\infty} = 1$ bar, $E=180\pm20$ J).....	<b>Error! Bookmark not defined.</b>
Figure 4.3: Run #12—Pressure distribution over shroud undersurface. ( $P_{\infty} = 1$ bar, $E=180\pm20$ J).....	<b>Error! Bookmark not defined.</b>
Figure 4.4: Run #12—Pressure distribution over focusing mirror ( $P_{\infty} = 1$ bar, $E=180\pm20$ J). Notice the influence of mechanical vibration on the pressure signal. ....	<b>Error!</b> <b>Bookmark not defined.</b>
Figure 4.5: Run #1—Pressure distribution over shroud undersurface. ( $P_6-P_9$ ; $P_{\infty} = 60$ mbar; $E_p=172\pm17$ J).....	<b>Error! Bookmark not defined.</b>
Figure 4.6: Run #1—Pressure distribution over focusing mirror. ( $P_{10-13}$ ; $P_{\infty} = 60$ mbar; $E_p=172\pm17$ J).....	<b>Error! Bookmark not defined.</b>
Figure 4.7: Run#7—Pressure distribution over shroud undersurface. ( $P_6-P_9$ ; $P_{\infty} = 150$ mbar; $E_p=222\pm23$ J).....	<b>Error! Bookmark not defined.</b>

Figure 4.8: Run#7—Pressure distribution over focusing mirror. ( $P_{10-13}$ ;  $P_{\infty}= 150$  mbar;  $E_p=222\pm23$  J).....**Error! Bookmark not defined.**

Figure 4.9: Run#11—Pressure distribution over shroud undersurface. ( $P_6-P_9$ ;  $P_{\infty}= 300$  mbar;  $E_p=231\pm23$  J).....**Error! Bookmark not defined.**

Figure 4.10: Run #11—Pressure distribution over focusing mirror. ( $P_{10-P13}$ ;  $P_{\infty}= 300$  mbar;  $E_p=231\pm23$  J).....**Error! Bookmark not defined.**

Figure 4.11: Data for blast wave front arrival time vs. Sedov's scaling law.....**Error! Bookmark not defined.**

Figure 4.12: Regions for impulse computation, using pressures measured during static tests.....**Error! Bookmark not defined.**

Figure 4.13: Run #1—Peak surface pressure vs. distance from laser line focus. ( $P_{\infty}= 60$  mbar;  $E_p=172\pm17$  J).....**Error! Bookmark not defined.**

Figure 4.14: Run#7—Peak surface pressure vs. distance from laser focal line. ( $P_{\infty}= 150$  mbar;  $E_p=222\pm23$  J).....**Error! Bookmark not defined.**

Figure 4.15: Run #11—Peak surface pressure vs. distance from laser focal line. ( $P_{\infty}= 300$  mbar;  $E_p=231\pm23$  J).....**Error! Bookmark not defined.**

Figure 4.16: Run#12—Peak surface pressure vs. distance from laser focal line. ( $P_{\infty}= 1$  bar;  $E_p=180\pm20$  J).....**Error! Bookmark not defined.**

Figure 4.17: Run #12- Blast wave evolution with measured surface pressures (top), and corresponding Schlieren image/frame timing (bottom).  $P_{\infty}= 1$  bar;  $E_p=180\pm20$  J. ....**Error! Bookmark not defined.**

Figure 4.18: Run #11 - Blast wave evolution with measured surface pressures (top), and corresponding Schlieren image/frame timing (bottom).  $P_{\infty}= 300$  mbar;  $E_p=231\pm23$  J.....**Error! Bookmark not defined.**

Figure 4.19: Run#7 - Blast wave evolution with measured surface pressures (top), and corresponding Schlieren image/frame timing (bottom).  $P_{\infty}= 150$  mbar,  $E_p=222\pm23$  J.....**Error! Bookmark not defined.**

Figure 4.20: LSD wave propagation followed by radial expansion;  $\alpha$  and  $\beta$  angles are indicated. *Left:* Run #8,  $P_{\infty}= 300$  mbar,  $E=205\pm21$  J. *Right:* Run #11,  $P_{\infty}= 300$  mbar,  $E=231\pm23$  J.....**Error! Bookmark not defined.**

Figure 4.21: Laser-induced breakdown with 2D model pitched forward 10-degrees. ....**Error! Bookmark not defined.**

Figure 4.22: The three zones and respective integration limits considered for the longitudinal impulse calculation. ....**Error! Bookmark not defined.**

Figure 4.23: Run #1—Peak surface pressure vs. distance from laser line focus. *Top*: Region 1; *Bottom*: Region 3. ( $P_{\infty} = 60$  mbar;  $E_p = 172 \pm 17$  J)**Error! Bookmark not defined.**

Figure 4.24: Run#7—Peak surface pressure vs. distance from laser focal line. *Top*: Region 1; *Bottom*: Region 3. ( $P_{\infty} = 150$  mbar;  $E_p = 222 \pm 23$  J)**Error! Bookmark not defined.**

Figure 4.25: Run #11—Peak surface pressure vs. distance from laser focal line. *Top*: Region 1; *Bottom*: Region 3. ( $P_{\infty} = 300$  mbar;  $E_p = 231 \pm 23$  J)**Error! Bookmark not defined.**

Figure 4.26: Run#12—Peak surface pressure vs. distance from laser focal line. *Top*: Region 1; *Bottom*: Region 3. ( $P_{\infty} = 1$  bar;  $E_p = 180 \pm 20$  J)**Error! Bookmark not defined.**

Figure 4.27: Momentum coupling coefficient vs. ambient pressure. (Assumes  $\Theta_{shroud} = 34$  deg.) ....**Error! Bookmark not defined.**

Figure 4.28:  $C_m$  variation vs. ambient pressure calculated for finite flat plate by Pirri (1973) and Richard (1989) vs. present experimental data from shroud undersurface (adjusted for shroud inclination). ....**Error! Bookmark not defined.**

Figure 5.1: Altitude vs. Mach number schedule for optimized airbreathing LP launch to low Earth orbit (Frasier, 1987). ....**Error! Bookmark not defined.**

Figure 5.2: Reynolds number variation with Mach number along optimized laser launch trajectory by Frazier (1987), together with T3 HST data from present test campaign. ....**Error! Bookmark not defined.**

Figure 5.3: Run 24—Typical HST and Pitot pressure signals obtained during experiments. ....**Error! Bookmark not defined.**

Figure 5.4: Run #1—Pressure transducer traces for Ch2-14 (distributed over 2D model); Laser ON, Flow ON;  $M = 8.61$ ;  $E_p = 196 \pm 20$  J. Channel number corresponds to

pressure sensor. Note simultaneous sensor response to laser-induced blast, indicating excessive mechanical noise. ....**Error! Bookmark not defined.**

Figure 5.5: Run #2- Pressure transducer traces for Ch2-14 (sensors distributed over 2D model); Laser OFF, flow ON;  $M=8.56$ ;  $E_p= 0$  J. The signal stability throughout the time window indicates fully established hypersonic flow over the model. ....**Error! Bookmark not defined.**

Figure 5.6: Run#0-Pressure transducer traces for Ch2-14 (sensors distributed over 2D model); Laser ON, flow OFF;  $M=7.8$ ;  $E_p=180\pm20$  J;  $P_\infty = 7.5E-02$  mbar. Note similarity to Run#1 results. ....**Error! Bookmark not defined.**

Figure 5.7: *Left*: Run #1—Erratic Schlieren image sequence . Note oversaturation of 2<sup>nd</sup> frame when laser induced breakdown occurred, and missing frames due to EMI. *Right*: Run #2—Schlieren image with laser OFF, revealing flow structure at  $M=8.56$ .....**Error! Bookmark not defined.**

Figure 5.8: *Left*: Diaphragm engraving geometry. *Right*: Burst diaphragm. ....**Error! Bookmark not defined.**

Figure 5.9: Run 10-Schlieren image with only the laser-induced air-breakdown glow visible. ( $M=8.77$ ,  $T_\infty=68.7$  K,  $P_\infty=0.15$  kPa).....**Error! Bookmark not defined.**

Figure 5.10: Run 10-Pressure gage traces for P6, P7,P9 distributed over shroud undersurface; laser ON, flow ON; Mach 8.77;  $E_p=207$ J. Sensor P9 pressure jump is from passage of blast wave.....**Error! Bookmark not defined.**

Figure 5.11: Run #13-Laser induced blast wave interaction with oblique shock. ( $M=5.95$ ,  $T_\infty=263.7$  K,  $P_\infty=5.62$  kPa,  $E_p=196\pm20$  J).....**Error! Bookmark not defined.**

Figure 5.12: Run#15-Laser induced blast wave interaction with oblique bow shock; -4° model pitch. The smearing of the focus is noticeable on the air-breakdown geometry. ( $M=5.95$ ,  $T_\infty=262.3$  K,  $P_\infty=5.16$  kPa,  $E_p=176\pm18$  J)**Error! Bookmark not defined.**

Figure 5.13: Run#16 - Laser induced blast wave interaction with oblique shocks from shroud and inlet center-body at 7.5° inclination. ( $M=5.96$ ;  $T_\infty=258.3$  K;  $P_\infty=5.32$  kPa;  $E_p=187\pm19$  J) ....**Error! Bookmark not defined.**

Figure 5.14: Run#16 - Measured pressure distribution over shroud under-surface; traces offset. Schlieren frames from Figure 5.13 are marked by diamonds. ....Error! **Bookmark not defined.**

Figure 5.15: Run#17 - Laser induced blast wave interaction with oblique shocks and shroud under-surface; 2D model at  $-7.5^\circ$ ; Shroud at  $-4^\circ$  inclination. (M=5.94,  $T_\infty=256.8$  K,  $P_\infty=6.25$  kPa,  $E_p=186\pm19$  J) ....Error! **Bookmark not defined.**

Figure 5.16: Run#17 - Long exposure color photograph of laser-induced breakdown geometry at Mach 5.96; 2D model at  $-7.5^\circ$ ; Shroud at  $-4^\circ$  inclination. ....Error! **Bookmark not defined.**

Figure 5.17 Run#17 - Measured pressure distribution across shroud under-surface. Traces offset. Schlieren frames from Figure 5.15 are marked for with diamonds. ....Error! **Bookmark not defined.**

Figure 5.18: Run#18 - Laser induced blast wave interaction with oblique shocks and shroud under-surface. Both center body and shroud at  $-7.5^\circ$  inclination. (M=5.94,  $T_\infty=284.4$  K;  $P_\infty=4.88$  kPa;  $E_p=121\pm12$  J) ....Error! **Bookmark not defined.**

Figure 5.19: Run#18 - Measured pressure distribution across shroud under-surface. Traces offset. Schlieren frames from Figure 5.18 are marked for with diamonds. ....Error! **Bookmark not defined.**

Figure 5.20: Run#19 - Measured pressure distribution across shroud under-surface; traces offset. Photon-drag detector signal provides timing for laser pulse delivery. ....Error! **Bookmark not defined.**

Figure 5.21: Run#20 - Extended duration pressure distribution over 2-D model, also showing transients before full flow establishment. Shroud sensors offset for clarification. (M=8.6;  $T_\infty=128.8$  K;  $P_\infty=0.566$  kPa;  $E_p=189\pm20$  J) Error! **Bookmark not defined.**

Figure 5.22: Run#20 - Pressure distribution over shroud under-surface showing P6, P7, P9 signals, masked by mechanical noise. Photon drag detector signal gives laser pulse timing (*bottom trace*). Pressure traces offset. .Error! **Bookmark not defined.**

Figure 5.23: Run#21 - Laser induced blast wave interaction with oblique inlet shocks and shroud under-surface. Model and shroud at  $-7.5^\circ$  inclination. (M=9.44,  $T_\infty=108$  K,  $P_\infty=0.301$  kPa,  $E_p=196\pm20$  J) ....Error! **Bookmark not defined.**

Figure 5.24: Run#21 - Long exposure photograph of bifurcated air-breakdown geometry across inlet gap, and secondary breakdown on shroud undersurface. ....**Error!**  
**Bookmark not defined.**

Figure 5.25: Run#21 - Measured pressure distribution across shroud undersurface; traces offset. Schlieren frames from Figure 5.23 are marked with diamonds. ....**Error!**  
**Bookmark not defined.**

Figure 5.26: Run#23 - Laser induced blast wave interaction with oblique shocks and shroud under-surface. Model at  $-7.5^\circ$  and shroud at  $-24^\circ$  inclination. ( $M=9.43$ ,  $T_\infty=113.7$  K,  $P_\infty=0.293$  kPa,  $E_p=106\pm11$  J).....**Error! Bookmark not defined.**

Figure 5.27: Run#23 - Measured pressure distribution at shroud under-surface; traces offset. Schlieren frames from Figure 5.26 are marked for clarification. ....**Error!**  
**Bookmark not defined.**

Figure 5.29: Peak pressures ( $\Delta P$ ) measured across shroud under-surface, measured from its leading edge. (Runs 16 through 19).....**Error! Bookmark not defined.**

Figure 6.1: Complete 2D model with full external compression inlet for Phase 2 tests. ....**Error! Bookmark not defined.**

Figure 6.2: Features to be added in 2<sup>nd</sup> generation 2D hypersonic models. ....**Error!**  
**Bookmark not defined.**

Figure 6.3: Axi-symmetric Lightcraft model ready for hypersonic tests in the T3 tunnel. ....**Error! Bookmark not defined.**

Figure 6.4: Pulsed power supply and 2.0 T magnet system.**Error! Bookmark not defined.**

Figure B.1: Logo for the collaborative effort set between RPI and HTN-LAH under sponsorship of the AFOSR.....**Error! Bookmark not defined.**

Figure C.1: Shock tunnel operation diagram. ....**Error! Bookmark not defined.**

Figure C.2: Reflected and transmitted shock after contact surface interaction, encountered in the reflected mode of operation ( $U_2=0$ ).**Error! Bookmark not defined.**

Figure D.3: Twin Lumonics TEA-922Ms and Schlieren setup in the laboratory....**Error!**  
**Bookmark not defined.**

Figure D.4: Panoramic view of the Laser Propulsion Laboratory. **Error! Bookmark not defined.**

Figure D.5: Schlieren montage of Lightcraft model #200 with beam centered, taken at 120,000 fps. .... **Error! Bookmark not defined.**

Figure D.6: Schlieren montage of Lightcraft model #200 with beam offset of 20 mm, taken at 50,000 fps. .... **Error! Bookmark not defined.**

Figure D.7: Integrated setup in the present 7.9 m x 5.2 m available laboratory space with altitude supersonic flow facility. .... **Error! Bookmark not defined.**

## ABSTRACT

The present research campaign centered on static and hypersonic experiments performed with a two-dimensional, repetitively-pulsed (RP) laser Lightcraft model. The future application of interest for this basic research endeavor is the laser launch of nano- and micro-satellites (i.e., 1-100 kg payloads) into Low Earth Orbit (LEO), at low-cost and “on-demand.” This research began with an international collaboration on Beamed Energy Propulsion between the United States Air Force and Brazilian Air Force to conduct experiments at the Henry T. Nagamatsu Laboratory of Aerothermodynamics and Hypersonics (HTN-LAH). The laser propulsion (LP) experiments employed the T3 Hypersonic Shock Tunnel (HST), integrated with twin gigawatt pulsed Lumonics 620-TEA CO<sub>2</sub> lasers to produce the required test conditions.

Following an introduction of the pulsed laser thermal propulsion concept and a state-of-the-art review of the topic, the principal physical processes are outlined starting from the onset of the laser pulse and subsequent laser-induced air-breakdown, to the expansion and exhaust of the resulting blast wave.

After installation of the 254 mm wide, 2D Lightcraft model into the T3 tunnel, static LP tests were performed under quiescent (no-flow) conditions at ambient pressures of 0.06, 0.15, 0.3 and 1 bar, using the T3 test-section/dump-tank as a vacuum chamber. Time-dependent surface pressure distributions were measured over the engine thrust-generating surfaces following laser energy deposition; the delivered impulse and momentum coupling coefficients ( $C_m$ ) were calculated from that pressure data. A Schlieren visualization system (using a high-speed Cordin digital camera) captured the laser breakdown and blast wave expansion process. The 2D model’s  $C_m$  performance of 600 to 3000 N/MW was 2.5-5x higher than theoretical projections available in the literature, but indeed in the realm of feasibility for static conditions. Also, these  $C_m$  values exceed that for smaller Lightcraft models (98 to 161 mm in diameter), probably due to the more efficient delivery of laser-induced blast wave energy across the 2D model’s larger impulse surface area.

Next, the hypersonic campaign was carried out, subjecting the 2D model to nominal Mach numbers ranging from 6 to 10. Again, time-dependent surface pressure distributions were recorded together with Schlieren movies of the flow field structure

resulting from laser energy deposition. These visualizations of inlet and absorption chamber flowfields, enabled the qualitative analysis of important phenomena impacting laser-propelled hypersonic airbreathing flight. The laser-induced breakdown took an elongated vertically-oriented geometry, occurring off-surface and across the inlet's mid-channel—quite different from the static case in which the energy was deposited very near the shroud under-surface. The shroud under-surface pressure data indicated laser-induced increases of 0.7- 0.9 bar with laser pulse energies of ~170 J, off-shroud induced breakdown condition, and Mach number of 7.

The results of this research corroborate the feasibility of laser powered, airbreathing flight with infinite specific impulse ( $I_{sp}=\infty$ ): i.e., without the need for propellant injection at the laser focus. Additionally, it is shown that further reductions in inlet air working fluid velocity—with attendant increases in static pressure and density—is necessary to generate higher absorption chamber pressure and engine impulse.

Finally, building on lessons learned from the present work, the future research plan is laid out for: a) the present 2D model with full inlet forebody, exploring higher laser pulse energies and multi-pulse phenomena; b) a smaller, redesigned 2D model; c) a 254 mm diameter axisymmetric Lightcraft model; and, d) a laser-electromagnetic accelerator model, designed around a 2-Tesla pulsed electromagnet contracted under the present program.

## 1. Introduction

Chemical rocket engines have been *THE* space launch “workhorse” technology ever since the dawn of the *Space Age* on October 4, 1957, when the former Soviet Union successfully launched Sputnik I. Now, a decade into the 21<sup>st</sup> century, it still remains the only propulsion technology available for Earth-to-Orbit (ETO) transport, with alternatives largely confined to paper studies, small lab experiments, academic exercises, and science fiction dreams. But why chemical rockets, and what makes *space access* so difficult?

As intriguing as it is, chemical rocket propulsion technology faces inherent problems that cannot be solved or mitigated. Take for example: 1) propellant explosion hazards—proven catastrophic on far-too-many occasions; 2) small propellant energy densities—i.e., the thermal energy released per unit mass of fuel; and, 3) performance is limited by physics—already “pressed up against the wall.” In short, such rocket physics is driven by thermochemistry and available chemical propellants, since ALL the energy required for the boost to orbit must be carried onboard. Even with the most energetic propellants we have—*i.e., the H<sub>2</sub>/O<sub>2</sub> reactive mix @ 20 MJ/kg (at stoichiometric ratio)*—chemical rocket launchers need propellant mass fractions of 0.90 (and higher) to reach low earth orbit. No technological breakthrough can change this picture dramatically, since modern 21<sup>st</sup> century chemical rockets already operate at efficiencies so high that *substantial* improvements are deemed physically unattainable.

Propulsion physics and propellant energy density not only drive performance of chemical rockets, but also the cost of operation—at best, \$10,000 per kilogram of cargo delivered to orbit. Launch costs haven’t significantly improved over the past half century and are not predicted to fall in the foreseeable future, regardless of incremental evolutionary change. To cut the cost of space access by 10x-100x, we need “game-changing” space launch technology. Presently on the horizon, the only candidate with this kind of potential is Beamed Energy Propulsion (BEP), and the physics is very well understood.

BEP is a “disruptive” technology that portends to complement, then later supersede chemical rockets, at least for micro/nano-satellite launch applications. In this concept, high intensity electromagnetic radiation is beamed from a remote radiation source (laser

or mm-wave) to a vehicle in flight, for direct conversion into thrust. Quite unlike chemical rockets, BEP takes its flight propulsive energy from this transmitted beam, rather than carrying it onboard as a massive fuel load. In airbreathing BEP engines, the working fluid is air, so thrust is produced by momentum exchange with the atmosphere; in the rocket BEP engines, thrust is produced by heating and expelling onboard propellant at a high velocity—no heavy oxidizer is needed, so low molecular weight propellants give exceptionally high specific impulse performance (e.g., 1000 to 2000 seconds or more).

By not having to lift the propulsive energy source in flight, BEP vehicles can leave the most heavy and expensive components on the ground as reusable power-plant infrastructure, for which the capital cost is amortized over copious launches. No highly reactive propellants are carried onboard, so the risk of catastrophic failure is minimal. The structural redundancy, safety equipment, and procedures that drive the mass and operational costs of conventional rockets upward, is neatly circumvented. Furthermore, BEP represents “green” transport technology that emits no pollutants during operation—100% environmentally friendly technology. Although *no* critical scientific or technological breakthroughs prevent the realization of BEP single-stage-to-orbit (SSTO) flights in the foreseeable future, the venture will require an arduous process of engineering adaptation. Plus, some of the critical technology apparently falls under ITAR or DoD restrictions.

Three potential liabilities of BEP (among others) must also be mentioned: 1) high initial cost and complexity of deploying requisite BEP infrastructure—multi-megawatt repetitively pulsed lasers (not available at this moment but within the realm of engineering feasibility); 2) transmitter adaptive optics for precise atmospheric turbulence compensation—“Star Wars” program spinoff, successfully applied in modern astronomical telescopes; and 3) eye safety—small glints (reflections) off Lightcraft engines could conceivably cause eye injuries at considerable downrange distances. To circumvent the last issue, laser launch facilities could be installed on remote, 3km high mountain peaks, employ source wavelengths that are “eye safe” (e.g., 1.62 um), and exploit boost trajectories that reduce reflected-beam intensity profiles to eye-safe

thresholds for all potentially affected populated areas (e.g., locate flight paths over sparsely populated deserts or the oceans).

The requisite BEP infrastructure is essentially a multi-megawatt class ground based laser (GBL) power station, which in the near term, would be designed for launching small satellites with payloads in the range of 1 to 10 kg (i.e., “nanosats”) into low earth orbit (LEO). As suggested above, adaptive optics, along with the appropriate choices of transmitter diameter and wave train characteristics (laser pulse energy, pulse duration, pulse repetition frequency, pulse shape, etc.) can minimize beam propagation losses through the atmosphere—an integral feature of the GBL power station. Although nanosatellite laser launchers would be the first natural step, once achieved, those technological foundations will soon enable more ambitious, 10x larger microsatellite payloads (10 to 100 kg). Ultimately, with a billion watts (~1GW) of beam power, payloads exceeding one tonne will become feasible, as proposed in the seminal work by **Kantrowitz (1972)**.

GBL launch stations offer high launch frequencies and short response times—an inherent strategic value that is hard to ignore (e.g., communications, surveillance, and intelligence needs). With GBL laser launchers, any part of the world is touchable in 50 minutes or less. Small payloads can be boosted on short notice and inserted into almost any desired orbit, or pitched into suborbital ballistic trajectories to any global destination. In fact, entire communications or navigation nano/microsatellites constellations could be launched “at will,” for low cost as suggested in **Kare, (1990)**, to replace recently negated military space assets.

BEP technology will eventually enable the visionary future applications outlined in **Myrabo and Ing (1985)** and **Myrabo and Lewis (2009)** that exploit both terrestrial and space-based power-beaming infrastructures. Imagine, for example, a global ultra-fast Lightcraft transportation system designed to replace the present congested hub and spoke commercial jet transport system, with ballistic launched Lightcraft flights linking any two cities on the planet. Imagine convenient flights to just about anywhere 50 minutes or less, operating from 100x to 1000x more “hub” airports than commercial airlines use today. The renderings in Figure 1.1 portray one such future Lightcraft port (left) and Lightcraft design (right) created by Palm.et.al.: the “LightPort” would function much

like a bus terminal today with no advanced reservations needed; the 5-m diameter Lightcraft vehicle, poised for liftoff, is sized to transport five people. These concepts were created in 2009 during a 10 week Masters-level design course at the Umea University Institute of Design, in Sweden, by one of 11 participating design teams.



Figure 1.1 Future application for BEP: worldwide transportation. Left: LightPort serviced by space-based power-beaming station. Right: Lightcraft vehicle on launch pad. Palm et al. (2009)

## 1.1 Worldwide State-of-the-Art on Beamed Energy Propulsion

Research on Beamed Energy Propulsion began in the early 1960's, right after the first high energy laser was invented, when scientists started investigating laser induced breakdown phenomena and plasma ignition, upon which the LP concept studied herein is based. As mentioned above, the concept for BEP earth-to-orbit launch was first proposed in 1972 by Arthur Kantrowitz, who claimed that a gigawatt ground-based laser could lift a 1 ton cargo into space (**Kantrowitz, 1972**). His work was closely followed by the first experiments on laser propulsion performed by **Pirri and Weiss (1972)** who worked with Kantrowitz at the AVCO Everett Research Lab in Everett, MA. That same year **Minovich (1972)** conceived an 'in-space' laser rocket system utilizing a remote laser power station.

These seminal events launched the *first wave* of worldwide Laser Propulsion (LP) research, along with related physics investigations. The sheer magnitude of relevant research produced in the past four decades, prevents all but the most recent to be mentioned here—most notably, those of relevance to the specific Laser Propulsion (LP)

concept pursued in the present research. For further reviews on seminal BEP work, see **Kare, (Ed.) (1987, 1990), Pakhomov, (Ed.) (2002, 2004, 2007)** and **Komurasaki, (Ed.) (2003, 2005)**.

In 1997, a new worldwide wave of laser propulsion research was triggered by the Myrabo-Mead Lightcraft flights at the White Sands Missile Range (WSMR) in New Mexico, using the PLVTS (Pulsed Laser Vulnerability Test System) 10-kW CO<sub>2</sub> laser (**Myrabo et al., 1998**). Myrabo's LP experiments demonstrated the viability of this highly-integrated, beam-riding pulsejet engine/vehicle geometry which evolved directly from his 1987 Lightcraft Technology Demonstrator (LTD) concept, developed for the Strategic Defense Initiatives Office (SDIO). As with other LP researchers, Myrabo's over-riding goal has been to cut space access costs by at least two orders of magnitude below the ~\$10,000/kg milestone of today's chemical rockets, while greatly improving reliability.

Of all the LP concepts that researchers worldwide have created over the years, many believe the *repetitively-pulsed laser thermal propulsion* concept is the closest to near-term ETO launch system realization. International teams in the USA, Russia, Japan, Germany, and China have investigated a wide variety laser pulsejet engine cycles (e.g., airbreathing Laser Supported Detonation (LSD) mode, Solid Ablative Rocket (SAR) mode, combined-cycle airbreathing/rocket modes, among others for a variety of different vehicle concepts). So far most of the research on the topic has been focused on the evaluation of the Momentum Coupling Coefficient ( $C_m$ ), which is a measure of how effectively id the incoming radiations transferred into kinetic impulse of the LP vehicle. This coupling coefficient is defined as the ratio between thrust and beam power ( $C_m=T/P$ ) for the case of continuous sources, given in units of N/MW. It can also be defined as the ratio between impulse and pulse energy ( $C_m=I/E_p$ ) for the case of pulsed sources, also given in units of N/MW.

Outside the USA's initial systems studies, several international LP research teams (e.g., in Germany, Japan, and ESA) have investigated the feasibility of commercial LP launchers for small payloads, while also exploring technical, economic, beam propagation, systems analysis and integration challenges. Even in countries just entering the field, BEP researchers universally recognize the revolutionary potential of laser

propulsion for low-cost space access. And judging from the rising list of Asian LP investigators in both Japan and now China, these teams are busy assembling resources to pursue LP launch technology; some interest clearly extends beyond purely academic research.

The following is a brief state-of-the art (SOA) review of global laser propulsion research relevant to near-term, nanosat/microsat laser launch systems.

### 1.1.1 United States

Pioneering LP research in the United States began in the 1970's and has evolved ever since. In the broadest sense, all laser electrothermal propulsion schemes can be classified as either Continuous Wave (CW) engines (**Nebolsine and Pirri, 2002**), or Repetitively Pulsed (RP) engines falling in three main categories: 1) Solid Ablative Rocket (SAR) (**Kare, 2002**); 2) Airbreathing (**Myrabo, 2002**); and 3) combined-cycle airbreathing/rocket (**Myrabo, 1987**).

In ablative laser rocket propulsion, an exposed solid propellant is rapidly vaporized by the incident laser beam, and thrust is generated as a result of the subsequent gas expansion process. Several alternative SAR concepts have been theoretically examined and experimentally demonstrated throughout the entire history of laser propulsion. Most recently, ablative laser propulsion studies were carried out at the University of Alabama by **Pokhamov et al. (2002)**. His investigations have screened a wide variety of materials (including lead, aluminum, Delrin®, Teflon®, water, ice, etc.) under different laser flux intensities, beam incidence angles, etc., searching for the optimum combination of momentum conversion efficiency and specific impulse. He has employed sophisticated diagnostics (including Schlieren imaging/visualization) to characterize the ablation process, mass consumption rates, blast wave velocities, and the like.

From the perspective of demonstrated beam-riding abilities, perhaps the most extensively explored laser propulsion concept to date is the Myrabo laser Lightcraft, in both its airbreathing and solid ablative rocket propulsion modes. Myrabo's initial BEP concept (**Myrabo, 1976**) proposed a single-stage-to-orbit (SSTO) shuttle concept based on a novel airbreathing magnetohydrodynamic (MHD) engine, powered by an orbital laser. As mentioned above, in the mid 1980's under contract to the Strategic Defense

Initiatives Office (SDIO), Myrabo's concept evolved to the Lightcraft Technology Demonstrator (LTD) concept—sized for launching 100 kg payloads to LEO—which lead to the Ph.D. thesis of **Richard (1989)** that theoretically analyzed the performance of its airbreathing pulsed laser detonation engine vs. altitude and Mach number.

Ten years later, Myrabo further evolved this LTD concept directly into an even simpler family of Lightcraft vehicles used in proof-of-concept flights at the High Energy Laser Systems Test Facility (HELSTAF) on White Sands Missile Range (WSMR). This free-flight test campaign (**Myrabo et al., 1998**) was carried out with 97.7 to 161.2 mm in diameter vehicles with masses up to 50 g, scaled to fly on the 10 kW PLVTS pulsed CO<sub>2</sub> laser. The 6061T6 aluminum vehicles with purely airbreathing pulse-detonation engines (i.e., infinite specific impulse) could fly up to 30 m altitude before the annular shroud melted/failed (**Mead Jr., 2007**). To resolve this issue and increase thrust by ~2.5x, a solid ablative rocket (SAR) version was created by inserting a thin band of Delrin (used as propellant) at the annular laser focus just inside the shroud, at the expense of a finite specific impulse. **Figure 1.2** shows a long exposure night-time photograph of an airbreathing Type 200 Lightcraft flight (right), along with an enlarged view of a stationary Type 100 Lightcraft (left) undergoing thrust stand tests (note the luminous laser-induced plasma exhaust expanding below the engine/vehicle).

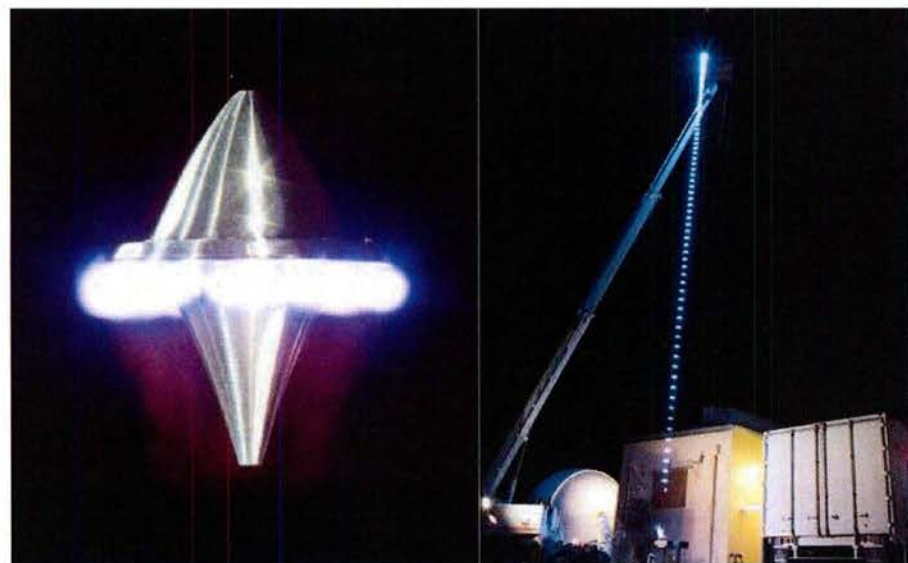


**Figure 1.2** Type 200 Laser Lightcraft in nighttime WSMR free-flight (right); Type 100 Lightcraft with expanding luminous air-plasma exhaust (left). (*Photos by James Shryne III—Courtesy of NASA*)

Sophisticated numerical LP research on the Lightcraft concept was conducted by (Wang et al., 2002) at the NASA Marshall Space Flight Center. His CFD simulations embody the most complete and complex axisymmetric numerical model of airbreathing Lightcraft engine physics attempted to date. Wang's model includes nonequilibrium thermodynamics and air-plasma finite rate kinetics, ray tracing, laser absorption and refraction by plasma, nonequilibrium plasma radiation, and plasma resonance. His code results have been extensively calibrated upon the experimental data of Myrabo et al. (1998) from WSMR laboratory tests of the Type 200 airbreathing Lightcraft engine. It is important to note that Wang's model simulates only a stationary airbreathing Lightcraft engine with a closed annular inlet, but it could, in principle, be extended to encompass an entire engine/vehicle flying at supersonic or hypersonic speeds through the atmosphere, with an open external-compression inlet, but MSFC has no current plans to pursue this objective.

BEP research at the AFRL Propulsion Directorate (Edwards Air Force Base, CA) has examined the energy conversion in LP engines—performed by Larson, et al. (2002), and the experimental/ numerical analysis of laser launch technology—conducted by Mead Jr., et al. (2005) and Knecht, et al. (2005). Larson studied the propellant chemistry, expansion process, and overall conversion efficiency: i.e., specifically the transformation of laser energy to ejected mass internal energy and exhaust kinetic energy, for SAR and airbreathing Lightcraft engines, assuming equilibrium and frozen flow. Mead Jr. et al. (2005) developed two scaled-up versions of the Myrabo Lightcraft: one 25 cm in diameter and the other, 50 cm (designated XL-25LR and XL-50LR, respectively). The objective was to deploy an actual vehicle for suborbital “sounding rocket” flights in the near term, subsequently followed by orbital launch attempts in the future. Static laboratory bench tests were conducted with the XL-25LR model, along with launch trajectory studies and other subcontracted hardware development (under SIBRs)—e.g., electronic systems and micro thrusters for attitude control and orbit circularization. SAR Lightcraft engines and small conical rocket nozzles were used to test the performance of different types of Delrin® (both black and white varieties), revealing minimal coupling coefficient differences. Trajectory simulations were performed for the X-25LR by Knecht et al. (2005) using the *Optimal*

*Trajectories by Implicit Simulation* (OTIS) numerical code, assuming a 1 MW GBL operating at 10.6  $\mu\text{m}$  with a beam power capture fraction of 82% into the combined-cycle pulsed LP engine. These simulated full-scale laser launches to LEO modeled the propulsion performance of both air-breathing and rocket phases of the flight trajectory.

Another critical research front is investigating the flight dynamics, stability, and control of repetitively-pulsed laser-propelled launch vehicles. One must clearly understand the beam-riding physics of existing and successful, spin-stabilized Lightcraft in order to acquire the wisdom to identify and create LP engine/vehicle configurations with exceptional merit and promise. In the near future, realistic/functional attitude control systems will be needed to maintain desired LP craft orientations and headings, in controlled flight along a launch trajectory to orbit.

**Kenoyer, et al. (2007)** have created a sophisticated, non-linear, 7 Degree of Freedom (7-DOF) flight dynamics model specifically for investigating the flight behavior of laser-boosted Lightcraft. The 7-DOF model, now precisely calibrated against 16 Lightcraft flights at WSMR, provides a realistic research tool for assessing beam-riding flight physics of innovative Lightcraft configurations that don't yet exist. The non-linear 6-DOF code incorporates all essential components (e.g., fully integrated engine, beam, aerodynamics, structures, and dynamics models), and permits such effects to be isolated so that the influence of any one may be studied separately and adjusted at will. Further RPI laboratory experiments with the Lumonics K922M laser system have measured the "beam riding" behavior of several engine LP configurations (e.g., Type #150, #200, and #250), using detailed diagnostics to record forces and moments, along with high speed Schlieren movies; these LP configurations were all previously flown at WSMR in test campaigns employing the 10-Kw PLVTS carbon dioxide laser.

Again, as mentioned earlier, several dozen research laboratories, institutes/centers, and universities—worldwide—have now investigated a staggering variety of concepts and applications for beamed energy propulsion: e.g., light sails, in-space laser-heated rockets, laser- and microwave energized airspikes—to name just a few. However, the present research emphasizes the SOA of basic research relevant only to the LP concept studied in this thesis.

### 1.1.2 Europe

European and Asian research in laser propulsion is relatively new and not so consolidated as in the United States and Russia. The German activity is centered in Stuttgart at the German Aerospace Center (DLR), and began right after Myrabo's successful WSMR indoor and outdoor flight experiments in 1997.

**Bohn and Schall's (2002)** initial research emphasized the interaction of high power CO<sub>2</sub> laser radiation with simple parabolic bell engines (see **Figure 1.3**), applying optical and other techniques to analyze the physics of breakdown and plasma generation. The static performance of their bell thruster, along with the Myrabo Lightcraft (#200-3/4) was tested with and without SAR propellants (e.g., Delrin®), at pressures ranging from sea level to a high vacuum. With DLR's high power CO<sub>2</sub> laser (11 µs pulse duration), their parabolic bell thruster clearly outperformed Myrabo's #200-3/4 Lightcraft engine in both airbreathing and SAR rocket modes. However, note that the bell geometry has not yet flown more than a second or two in free-flight, without the aid of wire guidance. In contrast, Myrabo's Lightcraft is a highly integrated vehicle/optics/engine platform for which stable "beam-riding" has already been achieved (a mandatory condition for successful free flights under laser power). The "German Lightcraft" has yet to demonstrate this essential feature beyond 5mm lateral offsets from the laser beam centerline.

Note also that the current Type 200 Lightcraft is simply the current baseline, proof-of-concept vehicle/engine that has flown outdoors on a laser waveform (i.e., pulse duration, PRF, and pulse energy—provided by the 10-kW PLVTS laser) that lies far outside the optimum requirements for this LP thruster. Further refinements in the plug-nozzle (i.e., off-axis parabolic) Lightcraft engine/vehicle, along with a more ideal laser source, will enable dramatic increases in engine performance throughout the subsonic, supersonic, and hypersonic regimes.

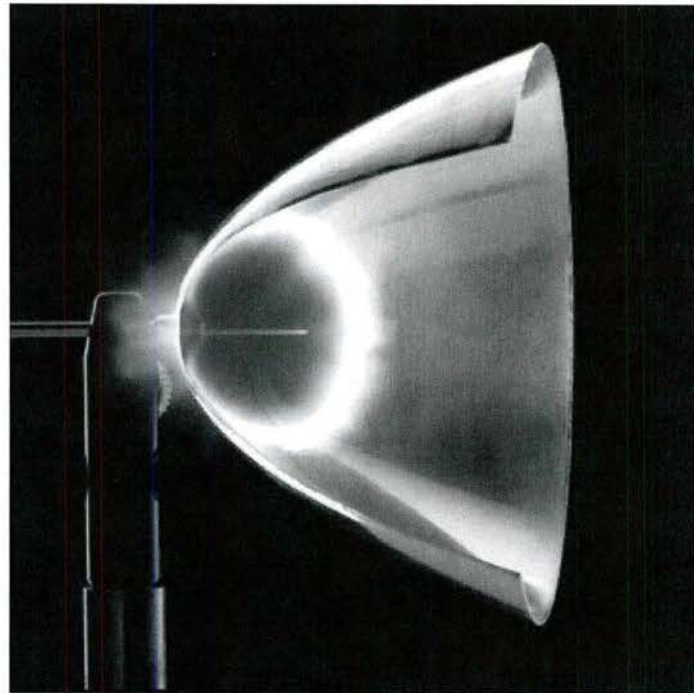


**Figure 1.3** Cutaway view of German “bell” engine, with ignition pin. Schall and Eckel (2003)

More recently, **Schall and Eckel (2003)** have continued their experimental research on parabolic aluminum thrusters, with brief wire guided and free-flights, ballistic pendulum tests, etc. In the wire-guided tests, model mass varied from 17 to 55 grams (to simulate a payload), while maintaining engine geometry and scale unchanged. An indoor flight altitude of 8 m was achieved with DLR’s repetitively-pulsed CO<sub>2</sub> electron discharge laser (175 J at 45 Hz, pulse width of 11  $\mu$ s) and the bell thruster in airbreathing mode, dynamically refreshed from the nozzle exit between pulses. Ballistic pendulum experiments were performed under various static pressures to simulate the effects of altitude upon the momentum coupling coefficient (C<sub>m</sub>).

In Portugal, **Resendes et al. (2004, 2007)** at the Instituto Superior Técnico in Portugal, under contract for the European Space Agency (ESA) performed an extensive review of laser propulsion SOA, and compared the applied LP research performed to date. The basic theory and concepts were also addressed. The work concludes with an analysis of the most promising concepts and provides suggestions for further experiments. Within this work, a basic first-order analysis of the trajectories and dynamics of the Myrabo Lightcraft was carried out (**Resendes et al., 2007**). This

analysis, which provides several insightful results, approximates the vehicle by a point-mass, with no beam-riding forces or moments; only the forces of gravity, drag, and thrust were simulated.

### 1.1.3 Japan

Outside the United States and Russia, Japan has produced the most extensive body of research on laser propulsion to date. Several renowned institutions have turned their attention to the concept in the last decade. Among them are: Tohoku University, the National Aerospace Laboratory, the University of Tokyo, Tokai University, and the Institute for Laser Technology (**Niino, 2002**).

**Komurasaki et al. (2002)** have performed numerical and experimental research on both laser and microwave propulsion concepts, addressing RP as well as CW thruster modes. Their numerical studies have investigated airbreathing, pulsed LP-ramjet schemes **Katsurayama, (2001)** with engine/vehicle geometries that closely resembled the Lightcraft Technology Demonstrator (LTD) concept proposed by **Myrabo et al. (1988)**. Various CFD analyses (see **Figure 1.4**) of this LP-ramjet concept have examined: 1) alternative Lightcraft forebody and shroud geometries, under various flight conditions (Mach number, ambient pressures/densities); 2) overall engine performance, and, 3) the influence of laser focal ring location upon laser energy conversion efficiency into thrust. One RP ramjet numerical model simulated the time-dependent behavior of a single thrust generating pulse. Another numerical model was built for CW laser rocket simulations to address the critical issues of wall heat losses, radiative losses, and laser absorption efficiency.

On the experimental front, **Mori et al. (2002)** and **Komurasaki et al. (2002)** linked a 10 J/pulse CO<sub>2</sub> laser system to a small-scale M=2.0 wind tunnel to investigate the laser-plasma expansion characteristics and blast wave production efficiency of a focused beam within the free stream. Also, a 2kW-class CW model thruster was built and tested, with the objective of measuring the efficiency of laser energy conversion into thrust.

Japanese researchers have also examined the feasibility of applying millimeter wave sources for beamed energy propulsion. **Nakagawa et al. (2003)** used a 1 MW gyrotron (operating in repetitive pulsed mode) to conduct proof-of-concept free flight and thrust

stand experiments with the airbreathing parabolic reflector model pictured in **Figure 1.5**. The momentum coupling coefficient ( $C_m$ ) performance generally fell in the same range as laser thrusters.

**Sasoh (2004)** introduced the Laser-driven In-Tube Accelerator (LITA) which is perhaps one of the most prominent Japanese concepts. Collaborative numerical and experimental research on the LITA concept has been carried out by Japan and South Korea investigators. As shown in **Figure 1.6**, a repetitively pulsed laser beam is projected down onto a primary mirror integrated with the vehicle forebody, then is refocused by the cylindrical secondary mirror (i.e., the shroud inner surface) to just underneath the vehicle. The projectile is propelled up the guide tube by a sequence of laser supported detonations that drive blast waves against the aft centerbody surface.

The launch tube may easily be filled with any propellant gas (e.g., air, nitrogen or argon). Hence, Sasoh's experiments have been performed with a variety of gas mixtures at various pressures, with the laser beam admitted either from upstream ("tractor beam" version as in **Figure 1.6** or downstream ("pusher beam" version) as in **Figure 1.7**, depending on the model tested. The breakdown threshold may be reduced as desired, through the choice of propellant gas. The noticeably higher  $C_m$  performance and impulse levels of LITA can be attributed to the tube's confinement effect, according to **Ohnishi et al. (2005)** who also performed a brief numerical analysis. Note that LITA is conceptually identical to one of Myrabo's 1983 "tractor beam" lightcraft designs reported in **Myrabo et al. (1983)** and **Myrabo and Ing (1985)**.

Seoul National University and Pusan National University, both in South Korea, have collaborated with the numerical analysis on Sasoh's LITA concept (**Sasoh, 2004**). The investigation, which retained the exact same vehicle/engine/optics configuration, examined the in-tube flight aerodynamic characteristics and internal flow field features (e.g., including the inlet unstarting process) occurring within LITA. Aerodynamic visualization experiments and subsequent analyses were also performed on the LITA model geometry in a supersonic wind tunnel (**Kim and Cho et al., 2002** and **Kim and Pang et al., 2002**).

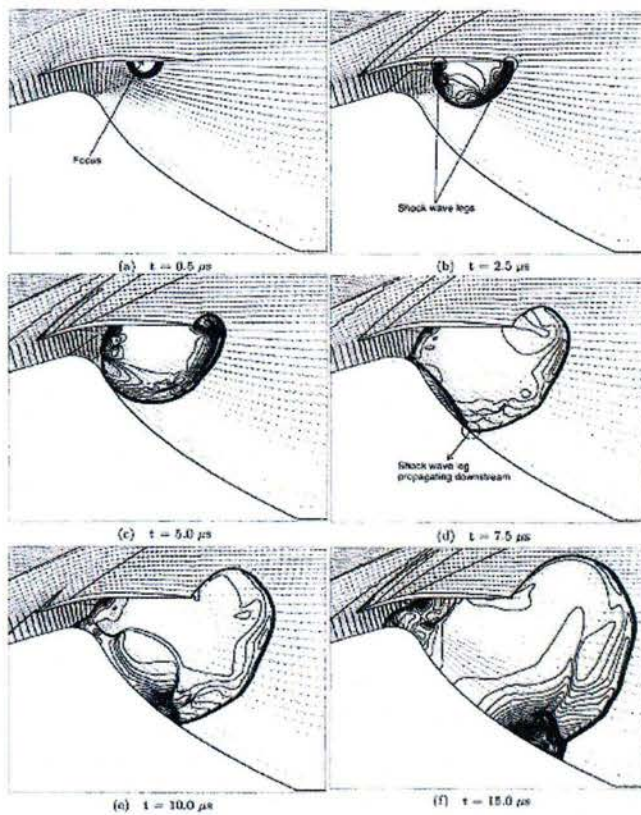


**Figure 1.4** Hypersonic ( $M=5.0$ ) CFD simulations of a 16 cm diameter Lightcraft flying at 20 km altitude. (Komurasaki et al., 2003)

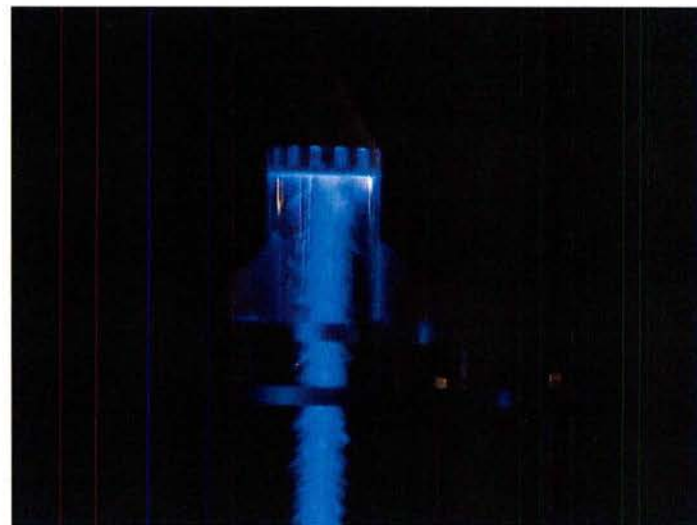


**Figure 1.5** Microwave-powered Lightcraft (Nakagawa et al., 2003)

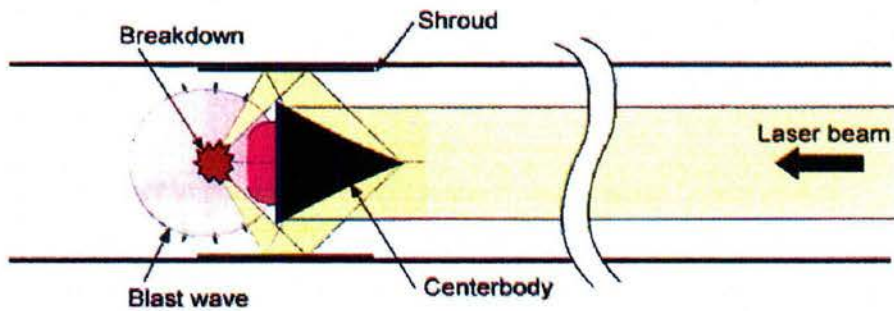


Figure 1.6 LITA concept, upstream beam operation (Komurasaki, 2002)

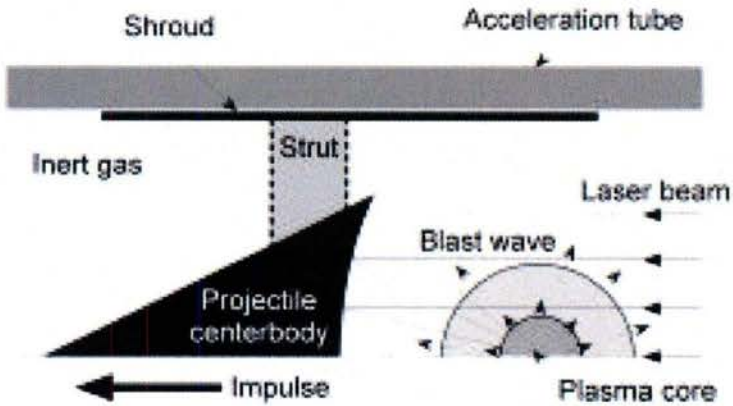


Figure 1.7 LITA features in a pusher beam configuration (Sasoh, 2004)

#### 1.1.4 Russia

Russians laser propulsion pioneers, as with the United States, also began their work in the early 1970's. Fundamental theoretical studies on laser-induced breakdown, and heating of gases by laser radiation had already been accomplished in the mid-1960's: e.g., the classical works of Raizer (**Raizer, Yu. P. (1965)** and **Raizer, Yu. P. (1966)**). Recent interesting works on the physics of laser propulsion include those by Apollonov (**Apollonov and Tishchenko, 2004a**, **Apollonov and Tishchenko, 2004b**, **Apollonov et al., 2005**) and Tishchenko (**Tishchenko et al., 2002**, **Tishchenko, 2003**). Apollonov proposed the use of a *pulse periodic mode* induced in high power gas dynamic lasers for the transmission of ultra-high PRF waveforms (while maintaining high pulse energy) into innovative LP engine concepts. Tishchenko's experimental and numerical research on moving Optical Pulsed Discharges (OPD) has shed insight into the conditions

necessary for successfully tailoring subsequent shock waves into the so-called Quasi-Stationary Wave (QSW) heating mode. In the QSW mode, a strong, almost planar shock wave is created by the merging of several shocks resulting from a high PRF laser-induced blast train. Significant improvements are claimed for the momentum coupling coefficient of QSM-heated engines, in comparison with the *no QSW tailoring* case, and experiments are underway to substantiate this assertion.



Figure 1.8 The ALSPE concept vehicle (Rezunkov et al., 2005)

**Rezunkov et al. (2005)**, another Russian research team, has conducted recent experiments with a novel AeroSpace Laser Propulsion Engine (ASLPE). This LP concept (see Figure 1.8) shares two features with Sasoh's LTIA "tractor beam" concept: 1) an axisymmetric forebody that serves as a primary receptive mirror, and, 2) an annular, ring-shaped secondary mirror. Note that ASLPE refocuses its annular beam *through narrow slits in its truncated conical nozzle* into a central laser absorption chamber; LITA has no such nozzle. The team claims: a) the unique engine geometry permits successful operation in both repetitively-pulsed (RP) and continuous wave (CW) propulsion modes, with roughly comparable efficiencies, b) optical windows are not required for the CW mode. Also demonstrated, was an inclined wire-guided flight of the ASLPE, propelled by a 6 kW repetitively-pulsed CO<sub>2</sub> laser (120J @ 50 Hz). Ballistic pendulum experiments with ASLPE gave momentum coupling coefficients (C<sub>m</sub>) in the

range of 25 to 40 dynes/W with that 6 kW RP laser, and 10 to 13 dyne/W with their 30 kW CW CO<sub>2</sub> laser.

### 1.1.5 Brazil

Brazilian interest in laser propulsion began in the 1990's and has, until recently, been focused largely on Directed Energy Air Spike (DEAS) research (**Minucci et al., 2003; Minucci et al., 2005; Oliveira et al., 2005; Salvador et al., 2008**) of relevance to streamlining hypersonic blunt forebodies. The DEAS concept employs beamed laser energy to create a "virtual spike" that diverts hypersonic airflow away from a vehicle's flight path, thereby reducing aerodynamic drag and heat transfer upon the blunt forebody. Experimental results have shown that hypersonic drag can be cut by as much as 40%. Investigations (see **Fig. 5**) are underway to quantitatively assess DEAS disruptions of established flow fields (**Oliveira et al., 2005**), and heat flux rates across blunt forebodies (**Salvador et al., 2008**).

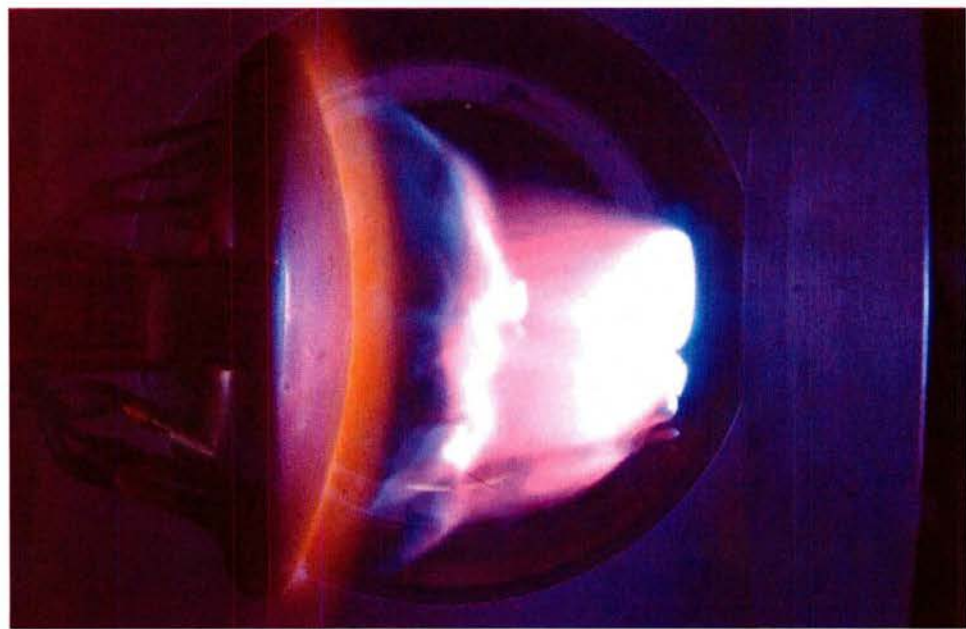


**Figure 1.9** Laser-induced DEAS hypersonic experiments in Brazil. (**Salvador, 2008**)

Hypersonic shock tunnels at the *Henry T. Nagamatsu Laboratory for Aerothermodynamics and Hypersonics* (HTN-LAH) in Brazil are linked to powerful CO<sub>2</sub> TEA lasers in preparation for ground-breaking LP experiments and related hypersonics research. HTN-LAH is the only research facility in the world capable of

simulating flow conditions inside (and around) LP ramjet and scramjet engines, with the capability of providing deposition of laser energy into the flow. The fabrication of several large-scale, two and three-dimensional LP engine segments and vehicles is presently underway, for which basic research experiments, of which this work is the first one of them, are being performed.

### 1.1.6 China

China has revealed a sharply increasing interest in laser propulsion, judging by their growing list of conference and journal articles published around the world. At present, this LP research appears constrained to experimental and theoretical studies of relevant basic physics issues, possibly retracing historical foundations laid down by USA, Russia, and other researchers. Some observers believe this work will soon blossom (if it hasn't already) into a formidable world presence in laser propulsion research.

**Cui et al. (2005)** with the Northwestern Polytechnic Institute at Xi'an, has carried out basic LP experiments and numerical simulations to investigate the effects of nozzle structure upon laser thruster performance. **Dou et.al. (2005)**, from the Zhuangbei Institute of Technology, conducted experimental research with a 100 J pulsed CO<sub>2</sub> laser to assess the impact of various gas mixtures upon the momentum coupling coefficient (C<sub>m</sub>) of simple laser thrusters. At the same institution, **Li et al. (2005)** examined the thrust generation mechanism within a RP thruster, comparing Sedov's self similar theory for strong explosions with numerical simulations of a single laser pulse focused at the centerline of a conventional nozzle.

At the University of Science and Technology of China, **Gong and Tang (2005)** performed a multi-pulsed simulation of an airbreathing bell nozzle thruster using FLUENT®. **Tang et al. (2005)** used a TEA CO<sub>2</sub> laser to conduct experiments on a parabolic thruster for a variety of pulse repetition rates and ambient pressures, within a vacuum chamber.

## 1.2 Motivation and Objectives

The work outlined in this thesis represents a solid initial “building block” for a future ambitious program that thoroughly investigates (both experimentally and

numerically) all LP propulsion modes and flight regimes encountered by a Lightcraft in its ETO flight, from liftoff to final orbit circularization. This thesis, to keep the research objectives both feasible and manageable, focuses on the Mach 7-10 laser scramjet regime which, represents a narrow portion of the entire Lightcraft flight trajectory, such as studied in (**Richards, 1989**) and (**Frasier, 1990**).

Extensive research into, and analyses of the subsonic/supersonic/hypersonic flight envelope facing a Lightcraft launch are clearly needed. Such investigations must include the consideration of novel engine/vehicle geometrical and design iterations that go well beyond the first embryonic Lightcraft concepts created (and available in the literature), as well as new trajectory profiles, laser beam parameters, beam propagation, infrastructure and cost analysis, and so on. All such needs will drive LP research objectives for years to come, of which the present thesis is just a first, but important step.

As briefly summarized in Section 1.1 above, prior research on airbreathing laser propulsion has been limited to: 1) stationary thrust stand tests; 2) short free-flights (some wire- and tube-guided) at low subsonic flight speeds; 3) laser energy deposition and static thrust generation studies (the most extensive studies), wherein the impulse and momentum coupling coefficients are measured with ballistic pendulums and/or load cells; and 4) numerical studies (very few of which are calibrated on real experimental data). These direct force/impulse measurements fail to reveal interdependent relationships between engine/optics/vehicle geometry, the blast wave expansion dynamics, and impulse generation process.

To adequately assess the impact of such Lightcraft geometrical features upon the impulse generation process—to a far greater extent than accomplished in past LP research—requires a completely different experimental technique, wherein: a) resultant impulse is measured by integrating time-variant pressure distributions created over engine surfaces; b) such pressure traces are correlated with high speed Schlieren movies that track positions of expanding, laser-generated blast waves; and, c) the time-variant thermal imprint of such laser-generated blast waves, as they expanded over the engine’s “hot section” and impulse surfaces, is recorded for subsequent analysis. The first item requires an array of appropriately placed piezoelectric pressure transducers over the Lightcraft model; the second item, a digital camera with a frame rate of 1000 fps or

better. To address the last item, in-depth knowledge of the distributed heat transfer load over the LP engine can be enabled with an array of heat transfer gages distributed/concentrated near the heavily loaded engine “hot section” surfaces.

Hence, now having in mind the limitations and advantages of pulsed laser propulsion, the SOA of previous LP research performed to date and the overall goals for future LP research, we can move forward to identify specific primary and secondary objectives for the present thesis research, as follows:

Primary Objectives:

- 1) Measurement of time-dependent surface pressure distributions over a 2-D Laser Lightcraft engine cross-section, including “hot section” (absorption chamber) and other internal surfaces;
- 2) Visualization of laser-induced blast wave expansions responsible for pressure increase —thus impulse generation—as well as its interaction with incoming hypersonic flow.

The first campaign would be conducted under quiescent air conditions at various ambient pressures up to 1 bar, to de-bug the complex experimental apparatus, and prepare for tests with flow. The second campaign would be performed at hypersonic flow conditions ranging from approximately Mach 6 to Mach 10. To secure the realization of these *primary objectives*, several complex apparatus and sophisticated tools must be made available and operational—thus leading to the *secondary objectives* given below.

Secondary Objectives:

- 1) *Develop and integrate the required experimental test facilities:* Link the HTN-LAH T3 Hypersonic Shock Tunnel with the Lumonics TEA-622 laser. This involved the transport (to Brazil), installation, and repair of the existing TEA-622 and the acquisition/design/manufacturing of the unavailable/needed equipment;
- 2) *Design, manufacture, and install 2D Lightcraft model:* This required the transport of the model to Brazil, insertion of pressure gages, installation of the model in the T3 tunnel, and de-bugging all instrumentation;

- 3) *Generate quality data for calibrating CFD tools:* The 2D model must give the kind of data needed to develop and calibrate sophisticated computational tools (CFD), for simulating design iterations and optimizing the LP engine concept;
- 4) *Determine airbreathing LP transition Mach numbers:* The Lightcraft concept under investigation, encompass a full-spectrum of LP propulsion modes that will transition from ramjet, to scramjet, and finally to rocket (i.e., using on-board propellant) modes along an earth-to-orbit launch trajectory. Hence, another secondary objective concerns the optimum transition points (i.e., Mach numbers) between operational modes, which is beyond this thesis. First is the LP subsonic-supersonic flow transition (analog to ramjet/scramjet transition), whereupon the inlet gap be widened to allow supersonic flow through the inlet throat. The second transition occurs when the LP scramjet inlet gap is closed at the upper limits of the sensible atmosphere—i.e., end of infinite specific impulse ( $I_{sp}=\infty$ ) regime—and the engine switches to the LP rocket mode.
- 5) *“Pave the way” for future, continuing research:* Once the present thesis campaign is concluded, the present work will be handed off as a legacy to other investigators, so that airbreathing LP research progress can continue unabated. At that point, the HST/laser facilities at IEAv-DCTA would be integrated and operational, well equipped for subsequent campaigns with the same or different LP models, and much extended regime of Mach numbers. The overriding goal is to avoid the (far-too-common) interval of “dead” scientific advancement, after a research campaign terminates—wherein all the time and effort spent assembling formidable new facilities, models, and tools is lost. Fortunately, the host organization for the present experimental research (IEAv-DCTA) has a long-range vision for LP, involving scientists and faculty at institutes in both Brazil and the USA, researchers with the interest and commitment to jump in, provide continuity, and keep advancing the SOA.

Even though the present thesis work has intended to tackle these questions and supply tentative answers, it is known a priori, that the closure to such issues lies far ahead. Years of arduous research will be required before solid, quantitative conclusions can be obtained. Hence, an overarching goal of the research presented herein is to foster

fertile grounds for future long-term research on the complex multidisciplinary science and technology of hypersonic airbreathing laser propulsion.

### 1.3 Thesis Outline

The main body of this dissertation is divided in 6 chapters. The first is an extensive review of the world-wide “state-of-the-art” in laser thermal propulsion, which motivated the present work and clarified its objectives. Chapter 2 introduces the phenomenology taking place within a laser Lightcraft’s absorption chamber, from the moment of laser beam influx to final expulsion of the laser-induced blast wave. It also introduces the theoretical impulse generation models used in the past by prominent researchers. Chapter 3 details the research facilities assembled and used, including the Hypersonic Shock Tunnel (HST), TEA CO<sub>2</sub> lasers, two-dimensional Lightcraft model, and all instrumentation assembled for the setup.

The experiments performed under static conditions at various ambient pressures are described in Chapter 4, wherein surface pressure measurements were acquired and used to assess the momentum coupling coefficient ( $C_m$ )—the defining figure-of-merit for any airbreathing laser propulsion engine. Together with the pressure measurements, Schlieren visualization of the breakdown phenomena and subsequent blast wave expansion was obtained.

The hypersonic portion of the experimental campaign is described and discussed in Chapter 5, covering simulated hypersonic flight conditions ranging from Mach 6 to 10. Time-dependent pressure distributions over the 2-D model’s impulse surfaces were measured; the interaction of laser-induced blast waves with engine boundaries and the established flow field was photographed and analyzed. Finally, the predominant conclusions extracted from all this acquired data are summarized here.

Logically, the appendix material follows the main body of the work: Appendix A covers the instrumentation and calibration procedures. Appendix B explains the international collaboration specifically set up between United States and Brazil for beamed energy propulsion research, which enabled the present work. Appendix C describes the basic flow modeling in a Hypersonic Shock Tunnel, aimed at the reader unfamiliar with this formidable experimental tool. Finally, Appendix D details some of

the work performed at RPI, where a dedicated laser propulsion laboratory was created. The vision for this laboratory is explained along with its capabilities, a few of the experiments performed to date, and others planned for the future.

## 2. Laser Induced Breakdown and Impulse Generation Process

The science of Laser Thermal Propulsion is a complex multidisciplinary affair involving quantum electrodynamics, optics, fluid mechanics, gas dynamics, high temperature plasma dynamics, and the like. Deep theoretical developments on such subjects lie beyond the scope of this thesis, so the interested reader is encouraged to seek out the original references for more thorough treatments than presented here.

In the present research, laser impulse generation and overall efficiency aspects are the principal foci. This chapter addresses the basic phenomena taking place following the laser energy deposition into a Lightcraft engine's absorption chamber, and the subsequent phenomena leading to the generation of impulse. These processes are laid out herein, in sequence, starting with pulsed laser illumination of the rear optic/afterbody, and finalizing with the blast wave exiting the engine boundaries.

As noted by **Raizer (1977)**, the laser spark generation process can be divided into three successive stages: 1) air breakdown, where ionization develops in the cold gas and the initial plasma appears; 2) interaction between the remainder of the laser pulse energy and the initially formed plasma, which includes the motion of the plasma front maintained by the laser radiation (e.g. LSD wave), heating of the plasma to very high temperatures, and absorption and reflection of the laser light by the plasma (plasma mirror effects); 3) formation of the detonation phenomena, resembling a small-scale nuclear fireball. Subsequently, the blast wave relaxes in an unpowered manner, delivering impulse while expending its strength, until it exits the engine/vehicle boundaries into the surrounding environment.

Section 2.2 below provides a cursory description of the essential physical processes, followed by Sect. 2.3 which gives a brief analytical formulation for impulse generation, leading to the principal LP engine performance parameters: a) Momentum Coupling Coefficient ( $C_m$ ), and, b) overall efficiency ( $\eta_o$ ). The  $C_m$  formulation is based on extensive theoretical work by **Pirri (1973)**, **Reilly et al. (1979)**, and **Richard (1989)**.

### 2.1 Early Stage – Cascade Ionization and Plasma Formation

The first step in laser energy absorption by a gas is the optical breakdown, which is characterized by a reduction of the molecular gas into ionized gas (plasma). Breakdown

of a gas by strong optical radiation is caused by two mechanisms (**Weil, 1989**): 1) cascade ionization (Inverse Bremsstrahlung - IB), and, 2) Multiphoton Ionization (MPI).

The first mechanism involves the absorption of laser radiation by electrons through collision with neutral particles, in a region in space subjected to a strong electromagnetic (EM) field and where free electrons (also called seed electrons) are present. These electrons will begin an oscillatory motion triggered by the EM field and collide with gas particles (with kinetic energy transfer), either increasing the random motion of the particles or causing energy losses by scattering, appearing as heat generation. If the electron kinetic energy is high enough, it can collide with a neutral molecule ionizing it on the impact, as described by **Eq. 2.1**



As shown, the result of the interaction is two slower free electrons, which repeat the process leading to an increase in the number of electrons in an electronic avalanche or cascade ionization process (Inverse Bremsstrahlung–IB). If the acting field is strong enough, breakdown occurs in the gas under consideration, otherwise loss processes slow down the avalanche preventing the formation of the breakdown. The necessary conditions are the existence of an initial electron on the focal volume, and that the acquisition by the electrons of an energy greater than the ionization.

The second process has a purely quantum nature and is typical of the optical frequency range. This process, called Multiphoton Ionization (MPI), occurs when electrons absorb simultaneously a certain number of photons ( $n$ ) with energy  $E_{\text{photon}} = h\nu$ , gaining enough energy ( $nh\nu$ ) to detach from atoms or molecules, which are then ionized. The condition for ionization is  $n = (E_i/h\nu) + 1$ , where  $E_i$  is the molecule ionization energy. This MPI process is described by **Eq. 2.2**



The probability of a multiphoton process is small, but increases with the light irradiance (photon flux). According to Weyl (1989), the importance of the MPI process is restricted to shorter wavelengths ( $\lambda < 1 \mu\text{m}$ ) and at CO<sub>2</sub> laser frequency ( $h\nu = 0.1 \text{ eV}$ ) is highly improbable, since ionization potentials of most gases are larger than 10 eV,

requiring simultaneous absorption of over 100 photons for the total energy ( $mhv$ ) to exceed the ionization potential. Both IB and MPI require laser irradiances higher than  $10^8$  W/cm<sup>2</sup> in gases, with this value decreasing to  $10^6$  W/cm<sup>2</sup> in the case of solids. Note that this considers actual gaseous environments, containing aerosols and other particulates, which aids in the breakdown process by being heated up under the laser irradiation and generating electrons by thermionic emission. For clean air devoid of any impurity, the breakdown threshold can be as high as  $10^{12}$  W/cm<sup>2</sup> for short pulses. Under normal conditions, there are over  $10^4$  particles/cm<sup>3</sup> larger than 0.1  $\mu$ m in the atmospheric air (**Reilly et al., 1977**), which acts towards the reduction of the breakdown threshold in atmospheric conditions.

In the present work, the laser breakdown is located on the inner surface of the Lightcraft's aluminum shroud, that leads to reduced breakdown thresholds, since the threshold for solids and liquids are significantly lower than that for gases. In the case of metal breakdown, plasma formation is preceded by metal vaporization, which occurs on thermally insulated defects with characteristic length of the order of  $10^{-6}$  m, which can attain temperatures higher than  $5 \times 10^3$  K (for  $I \sim 10^8$  W/cm<sup>2</sup> and  $\tau \sim 5 \times 10^{-8}$  s). (**Walters et al., 1978**).

### 2.1.1 Metal Surface Air-Breakdown

As pointed out by **Walters et al. (1978)** and **Weil (1989)**, plasma ignition on a metallic target surface occurs at the rising portion of the beam pulse profile spike, with the plasma formation preceded by surface vaporization, following absorption of the radiation in a skin depth on the order of  $10^{-10}$  angstroms. With a pulse width of tens of nanoseconds (as with the present experiments), the thermal diffusion length is much larger than the skin depth, so the surface temperature is given by

$$T = T_0 + \left( \frac{2I\alpha}{K} \right) \left( \frac{\chi t}{\pi} \right)^{\frac{1}{2}} \quad (2.3)$$

Assuming the interaction of a clean aluminum surface and a CO<sub>2</sub> laser pulse ( $\lambda = 10.6$   $\mu$ m), absorptivity ( $\alpha$ )  $\sim 0.05$ , thermal conductivity ( $K$ ) = 2.4 W/cm, and thermal diffusivity ( $\chi$ ) = 1 cm<sup>2</sup>/sec, and considering the laser irradiance ( $I$ ) as  $10^8$  W/cm<sup>2</sup> and

pulse time of  $(\tau_p) = 5 \times 10^{-8}$  s, **Eq. 2.3** yields  $T-T_0=500$  K, which is lower than the melting temperature for the metal. This shows that the ignition occurs on thermally insulated defects of thickness  $d= 0.1$  to  $0.3$   $\mu\text{m}$ , which is much smaller than the thermal diffusion depth and has its temperature is governed by the equation

$$T = T_0 + \frac{I\alpha t}{\rho C d} = T_0 + \frac{0.0102}{d} \quad (2.4)$$

where  $\rho$  and  $C$  are the density and specific heat of aluminum, respectively. Under the same circumstances ( $d = 2$   $\mu\text{m}$ )  $T-T_0=5100$  K, a temperature rise high enough for vaporization within the laser pulse spike.

Modeling of the breakdown initiated on metal (Al) surface defects was first examined by **Weyl et al. (1980)**. This model assumes a three-part event sequence, following laser energy deposition: 1) evaporation of thermally insulated metal flakes, 2) laser induced breakdown in the metal vapor with a 1-D expansion, and, 3) breakdown with a 3-D expansion of the vapor in later times. It is stipulated that breakdown threshold depends on the ratio of vaporization temperature to the ionization energy, which in turn determines the initial electron concentration required for the inverse Bremsstrahlung -- and it is time dependent, varying with the incident irradiance, as shown in **Figure 2.1**. If the breakdown is sufficiently rapid ( $I > 10^8$  W/cm<sup>2</sup> for Al at 10.6  $\mu\text{m}$ ) the expansion can be treated as one-dimensional. For lower intensities, three-dimensional effects become important due to previous over expansion of the vapor and later onset of the breakdown in the vapor behind the shock.

The presence and size of defects (flakes) depend on the mechanical properties and method of preparation for the surface; both play pivotal roles in the surface-initiated breakdown process. Surface preparation has proven important in recent experiments performed at RPI with aluminum Lightcraft engines that demonstrated higher impulse from increasing the surface roughness (by sanding) around the laser focus. A simple explanation for this effect can be postulated: With a reduction in initial breakdown energy, a larger portion of the total incident laser energy is deposited into the local air plasma, thus increasing the subsequent blast wave's strength. Faster breakdown times means less laser energy reaches the surface prior to the onset of absorption by the

attached gas layer. Enhanced early breakdown might also reduce wall heating at the focus; however, future research must verify this hypothesis.

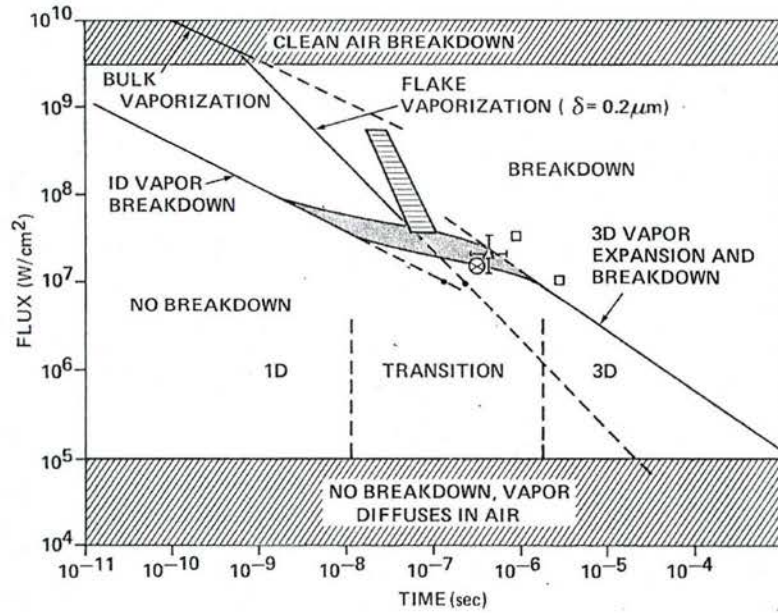


**Figure 2.1: Breakdown threshold dependence on incident radiation for Al at 10.6  $\mu\text{m}$ , and characteristics times for breakdown initiation. Weyl et al. (1980).**

The laser energy spent on electrical breakdown of the aluminum surface can likely be neglected in the present experiments, even though the laser focus “burn” (about 1 mm wide and 12.5 cm long—a surface area of only  $1.25 \text{ cm}^2$ ) upon the shroud is clearly distinguishable after several laser shots. At the irradiance levels necessary for flake vaporization,  $I > 10^9 \text{ W/cm}^2$ , only  $10^{-9} \text{ s}$  (see Fig. 2.1) is invested on breakdown or about 1/100th of the energy available in the  $\sim 100 \text{ ns}$  pulse width (FWHM) obtained in the present experiments. Hence, the inner surface of the shroud serves not as an ablatant, but as a catalyst for enhancing surface air-breakdown—a kind of “spark plug” that ejects free electrons into the gas to trigger air breakdown and expedite the ignition of LSD waves. Close examination of the focal burns during the present campaign reveals that negligible mass had been ablated from the shroud along the focus.

## 2.2 Post-Breakdown Phenomena and Absorption Waves

Following the initial stages of plasma formation, several transient phases take place throughout the plasma evolution sustained by the laser, during the pulse. The nature of

the plasma and resulting effects over the ignition surface are a function of the ambient atmosphere, irradiance, pulse duration, and wavelength. Depending on these parameters, three types of plasma waves can be observed to propagate into the surrounding atmosphere: 1) Laser Supported Combustion (LSC) waves; 2) Laser supported Detonation (LSD) waves; and 3) Laser Supported Radiation (LSR) waves. These three different absorption waves can be distinguished on the basis of their propagation velocity, pressure and expansion process during the subsequent plasma evolution process.

Following the hot vapor formation and initial plasma generation over a surface, the plasma becomes strongly absorbing and interacts with the surrounding air in two ways (**Root, 1989**): 1) rapid expansion of the high pressure vapor, driving a shock wave into the atmosphere, and 2) energy transfer to the atmosphere by a combination of thermal conduction, radiative transfer (i.e., re-radiation), and shock wave heating. For the high laser irradiance levels encountered throughout the present research, shock heating of the adjacent atmosphere dominates as adjacent gases that were previously transparent to the beam (when cold), start to absorb the laser radiation.

With the creation of an absorbing gas layer, the plasma becomes a fully developed propagation wave, absorbing most of the laser energy in its advancing front while shielding the remaining plasma from direct laser interaction. Such absorption waves propagate towards the laser source until the beam is terminated, or the irradiance falls to levels insufficient to support the absorption wave (**Raizer, 1977**).

The general configuration of an absorption wave is sketched in **Figure 2.2** (applicable to all 3 types) which identifies the principal zones and their evolution in time. Radial expansion of the plasma is always present but can be considered negligible in comparison with the axial plasma propagation effects; however, when the rarefaction waves begin to coalesce into the central axis, they dominate the evolution of the plasma at the surface. The radial expansion effects upon the propagation zone front (if any) are dependent on the nature of the propagation mechanism (i.e., LSC, LSD, or LSR).

**Table 2.1** summarizes the main differences between these three absorption wave propagation regimes. **Figures 2.3** and **2.4** give idealized, qualitative illustrations of the differences in a one-dimensional reference frame, highlighting the distinct gasdynamic

regions (from ambient to the wall) and dominant characteristics of each type, together with variations in gas velocity, pressure, temperature, and density. Although highly idealized representations, they still provide a clear first-order representation of the underlying physics.

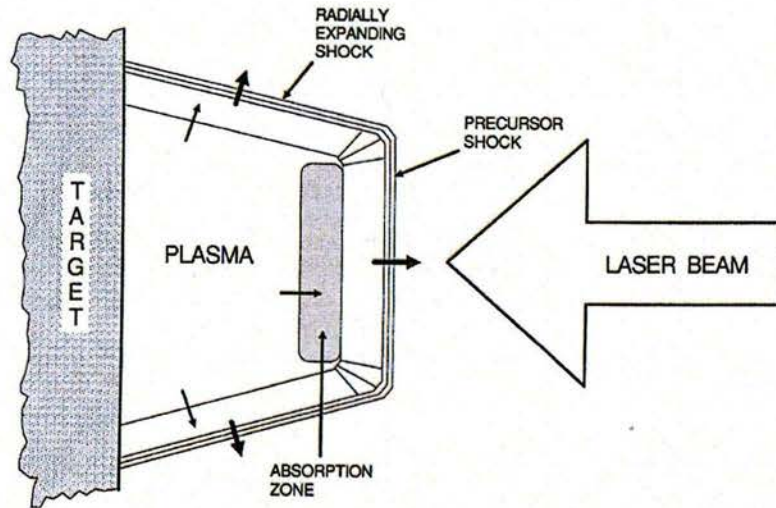


Figure 2.2: Absorption wave zones of a laser supported plasma from a metallic surface. (Root, 1989)

**Table 2.1: Laser-supported absorption wave propagation modes (10.6  $\mu\text{m}$  radiation).**

Propagating Absorption Wave	General Features
<b>LSC – Laser Supported Combustion</b>	<ul style="list-style-type: none"> <li>- Low laser Irradiance (<math>I &lt; 10^7 \text{ W/cm}^2</math>);</li> <li>- Precursor shock separated from centimeters-thick absorption zone and plasma;</li> <li>- Analog to 1-D chemical deflagration wave;</li> <li>- LSC wave advances at supersonic speed in the laboratory frame, but subsonic relative to precursor shock;</li> <li>- Thermal conduction and radiation as propagation mechanisms;</li> <li>- Equilibrium heating process.</li> </ul>
<b>LSD – Laser Supported Detonation</b>	<ul style="list-style-type: none"> <li>- Occurring at intermediate irradiance levels (<math>10^7 &lt; I &lt; 10^9 \text{ W/cm}^2</math>);</li> <li>- Millimeters-thick absorption zone follows directly behind precursor shock, with shocked gas at sufficiently high temperature to absorb laser energy directly → analog to chemical detonation wave;</li> <li>- Supersonically advancing LSD wave;</li> <li>- Non-equilibrium heating process (two temperature gas; electrons @ 2-3+ ev) gives lower temperature ions and neutrals than with LSC waves.</li> </ul>
<b>LSR – Laser Supported Radiation</b>	<ul style="list-style-type: none"> <li>- Highest level of irradiance (<math>I &gt; 10^9 \text{ W/cm}^2</math>);</li> <li>- Ambient gas heated to light absorption temperatures prior to shock arrival;</li> <li>- Low pressure increase, but high temperature increase (taking place at constant pressure);</li> <li>- Non-equilibrium heating process (two temp. gas)</li> </ul>

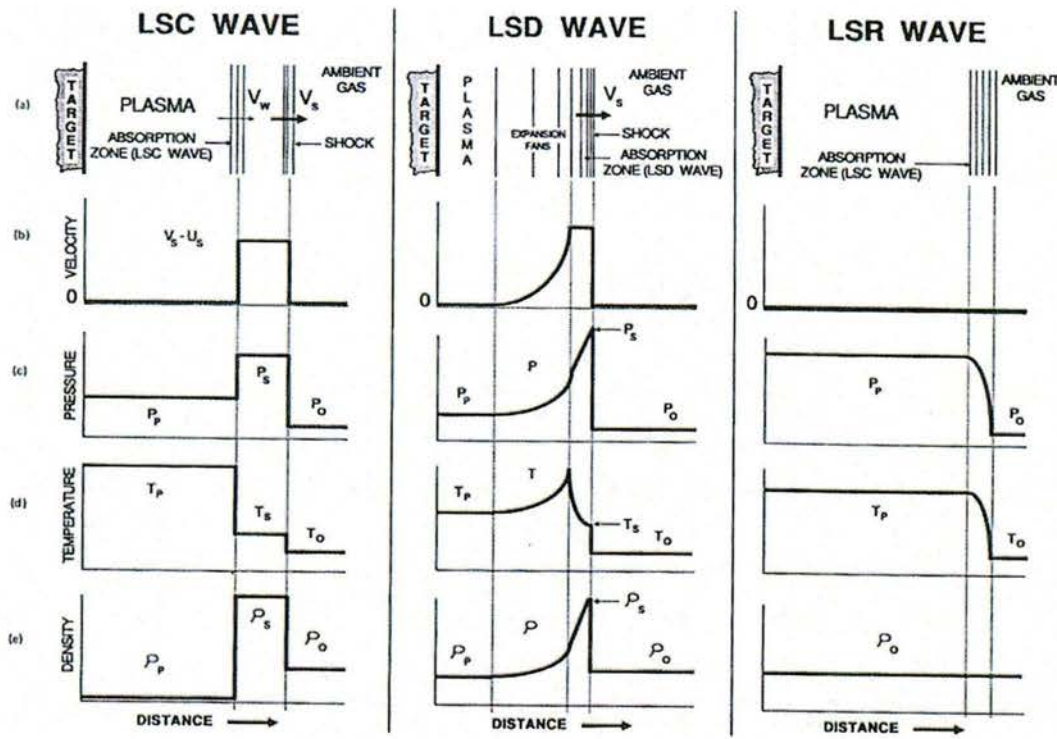


Figure 2.3: One-dimensional propagating plasma regions following laser absorption waves. (Root, 1989)

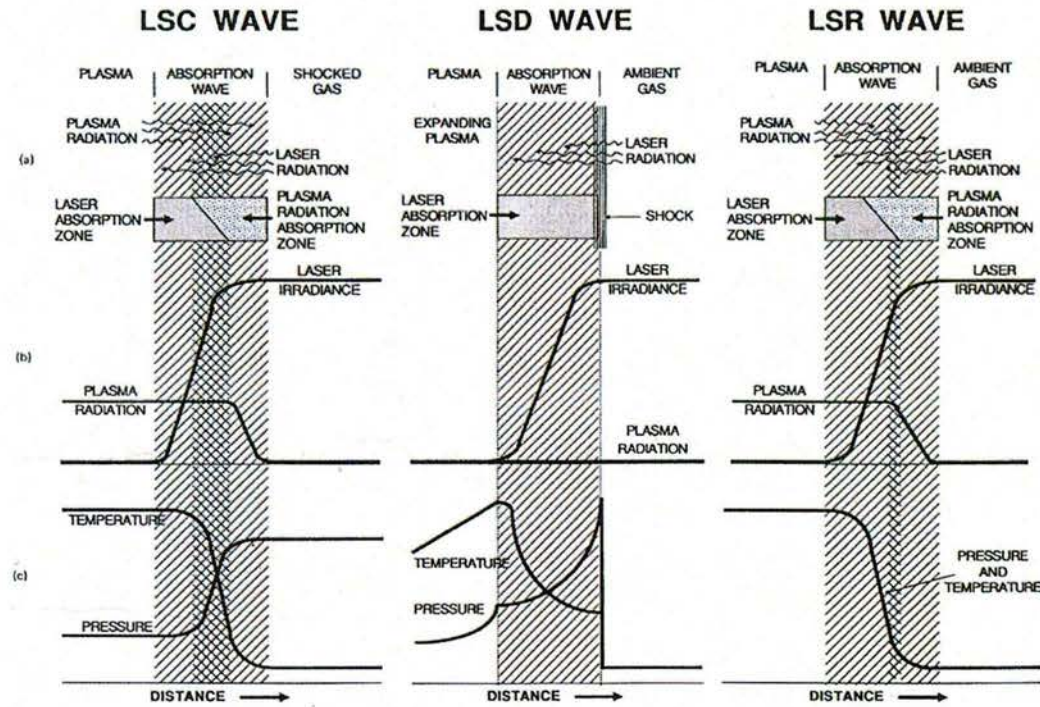


Figure 2.4: Absorption regions of the one-dimensional waves. (Root, 1989)

Previous studies on laser-supported absorption waves ignited off aluminum surfaces have observed the onset of LSC waves in irradiance levels as low as  $3 \times 10^4 \text{ W/cm}^2$  for CO<sub>2</sub> lasers at 10.6 μm (Reilly et al., 1979). In the present experiments, an analysis of our Lumonics TEA622 laser pulse profile shows that intensities in the order of  $10^8 \text{ W/cm}^2$  are achieved at the line focus, throughout most of the pulse. Henceforth, it can safely be assumed that LSD waves are the only powered type of absorption waves taking place here.

Raizer (1965) was first to model LSD wave propagation by comparing it to a chemical detonation wave, wherein the laser heats up the gas immediately behind the advancing shock wave, until the local gas velocity becomes sonic at the Chapman-Jouget (C-J) point. LSD wave propagation speed is determined by laser energy deposited between the shockwave and the C-J point; behind the C-J point the behavior is uncoupled, with no effect on the propagating plasma.

Initial gas/plasma properties before the rapid absorption are given by the shock wave jump conditions. LSD plasma conditions can be assessed by assuming conservation of momentum, mass and energy at the C-J point, and the complete absorption of laser power. Here, the shock velocity  $V_s$  is identical to the LSD wave speed, as given by (Raizer, 1965, 1966, 1977; Zeldovich and Raizer, 1966; Root, 1989)

$$V_s = \left[ \frac{2(\gamma^2 - 1)I_0}{\rho_0} \right]^{1/3} \quad (2.5)$$

The LSD wave properties are characterized by their values at the C-J point, with the density ( $\rho_s$ ), pressure ( $p_s$ ) and enthalpy ( $h_s$ ) given as

$$\rho_s = \frac{\gamma + 1}{\gamma} \rho_0 \quad (2.6)$$

$$p_s = \frac{\rho_0 V_s^2}{\gamma + 1} = \frac{[2(\gamma^2 - 1)I_0 \sqrt{\rho_0}]^{2/3}}{\gamma + 1} \quad (2.7)$$

$$h_s = \frac{\gamma^2}{(\gamma-1)(\gamma+1)^2} V_s^2 \quad (2.8)$$

For an LSD wave propagating away from a wall, the effects of that surface must be included. Behind the C-J point, expansion fans will appear which permit the gas velocity to drop to zero at the wall (Pirri, 1973, 1978; Reilly et al., 1979). These properties at the wall are determined by isentropic expansion through the rarefaction waves, with the values at the wall given by

$$p_w = p_s \left( \frac{\gamma+1}{2\gamma} \right)^{\frac{2\gamma}{\gamma-1}} \quad (2.9)$$

$$\rho_w = \rho_s \left( \frac{\gamma+1}{2\gamma} \right)^{\frac{2}{\gamma-1}} \quad (2.10)$$

$$h_w = h_s \left( \frac{\gamma+1}{2\gamma} \right)^2 \quad (2.11)$$

Although the above equations neglect real gas effects (excitation, dissociation and recombination) and heat transfer losses, they nonetheless provide insight to the essential physics. In the present research, these equations enable first-order initial estimates for the surface pressures near the focal line on the Lightcraft shroud, which drove the selection of pressure transducers purchased for the present 2D laser scramjet experiments.

**Root (1989)** also notes that his theoretical models do not account for laser beam angle of incidence relative to the surface. His one-dimensional analysis assumes that both the LSD wave and leading shock propagate away normal to the target surface, whereas at later times when the initial transient from plasma initiation has died out, the LSD wave propagates up the beam axis towards the laser source.

Likewise, in the present 2D laser scramjet experiments, breakdown occurs at the shroud undersurface, subsequently igniting a LSD wave that cuts a wedge-shaped swath across the supersonic inlet in roughly 1.5  $\mu$ s (i.e., the laser pulse duration); the laser

beam centerline is oblique to the shroud undersurface. This LSD-wave powered portion of the laser propulsion cycle, resembles a pulsed “planar heater” (wedge-shaped, actually) that slices across the supersonic inlet air working fluid, producing a strong blast wave that subsequently expands and decays during the unpowered portion engine cycle. This unpowered blast wave expansion is responsible for the great majority of the impulse generation in this pulsed detonation engine. The extremely high pressure LSD wave momentarily acts on only a very small region/volume of absorption chamber air, over a time span orders of magnitude shorter than that of the unpowered blast wave expansion.

### 2.3 Analytical Model of Surface Pressure History and Impulse Generation

Presented below is a first-order theoretical analysis of the laser-induced pressure distribution across a flat impulse surface, analogous to the thruster surface considered in the present pulsed LP scramjet experiments. This theory will later be applied to the analysis of pressure transducer data acquired in the initial experiments carried out under static (i.e., no flow) conditions. A more extensive and general development of the theory for laser-generated impulse, imparted to a surface under static atmospheric conditions, can be found in the works of **Pirri (1973)**, **Reilly et al. (1979)**, **Reilly et al. (1984)** and **Richard (1989)**.

The basic objective of the theory presented here is the quantitative prediction of the momentum coupling coefficient ( $C_M$ ) in a laser irradiance regime where a Laser Supported Detonation (LSD) wave launches a subsequent unpowered blast wave that dominates the momentum transfer process. This process begins with the onset of local air breakdown at a moment  $t << \tau_p$ , where  $\tau_p$  is the laser pulse duration, followed by the LSD wave propagation and extinction at  $\tau_p$ . The impulse generated during this process is small due to the short,  $\sim 1\mu\text{s}$  pulse duration, as will be shown later. Following next, is the unpowered blast wave expansion, driven by the piston-like behavior of the LSD wave, wherein the impulse magnitude can be calculated from the gas dynamic motion of the relaxing blast wave using self-similar relations. As initially developed by **Pirri (1973)**, the blast wave motion is modeled by matching an analysis of the one-dimensional shock

dynamics to the relaxing blast wave model, including two-dimensional expansion effects, as described in **Reilly et al. (1979)**. The surface pressure and impulse are then calculated as a function of time as the blast wave propagates over and away from the flat impulse surface.

The dominant time scale in the problem is the total time ( $\tau_0$ ) over which impulse is delivered to the surface. Under the action of the laser pulse, the initial motion of the LSD wave can be modeled as one-dimensional propagation, turning into a two-dimensional propagation once the leading edge of the rarefaction fan initially at the laser spot edge, propagates to the centerline. This characteristic time is given by

$$\tau_{2D} = \frac{R_s}{V_s} \quad (2.12)$$

where  $R_s$  is the spot radius and  $V_s$  is the LSD wave speed. Slightly different definitions are given for the value of  $\tau_{2D}$  in the literature.

Thus, the impulse delivered to the thruster surface consists of the combined contributions from a) when the laser pulse is on, and b) after the laser pulse has terminated. While the laser pulse is on ( $t \leq \tau_p$ ), the impulse contribution per unit area can be given by

$$\frac{I}{A} = \int p dt = p_w t \quad (2.13)$$

For short pulses ( $\tau_p < \tau_{2D}$ ), the relaxation is assumed to take place in a one dimensional form until  $\tau_p = \tau_{2D}$ , with the propagation becoming two-dimensional before the gas pressure decays to ambient. **Pirri (1973)** and **Reilly et al. (1979)** adopt a two-dimensional model for the initial blast wave propagation assuming a circular spot area over the surface leading to a cylindrical high pressure plasma generated by the one-dimensional LSD propagation towards the laser source. The unpowered cylindrical expansion laws developed by **Sedov (1951)** are then used to model the blast wave expansion and relaxation: i.e., the surface pressure versus time history.

**Richard (1989)** uses the same cylindrical blast wave expansion laws, but models the plasma formation along a line focus lying on the impulse surface (see **Figure 2.5** below), assuming this LSD-generated plasma takes on a horizontal semi-cylindrical

geometry over the impulse (target) surface. An unpowered blast wave is then assumed to be launched from the leading edge of the LSD wave upon laser pulse termination. This geometrical configuration more closely resembles to the impulse generation geometry in the present Lightcraft engine experiments. The two cylindrical configurations are compared in **Figure 2.5** below.

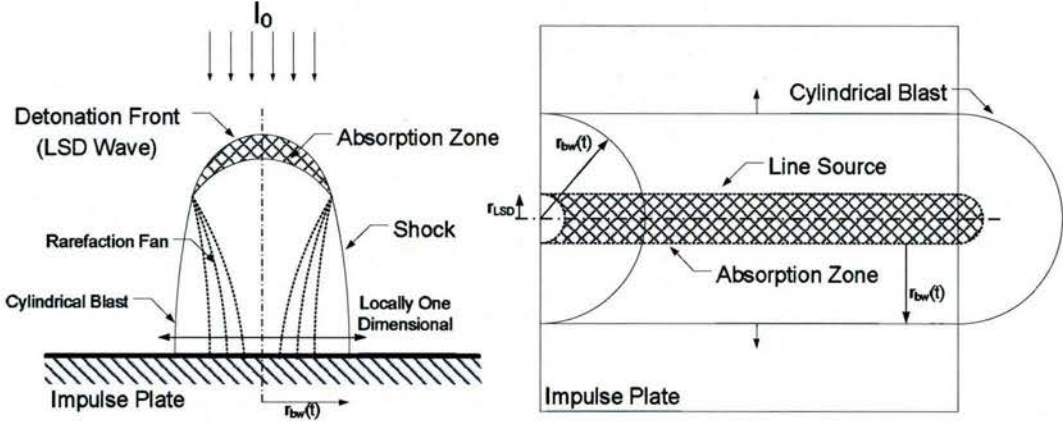


**Figure 2.5: Cylindrical blast wave expansion models. Left: vertical oriented axis; Right: horizontal oriented axis (following laser-induced surface breakdown).**

Then  $t = \tau_{2D}$ , the surface pressure for the case of  $\tau_p \leq \tau_{2D}$  can be defined as

$$P_{w(\tau_p \leq \tau_{2D})} = p_w \left( \tau_p / \tau_{2D} \right)^{\frac{2}{3}} \quad (2.14)$$

And when  $t > \tau_{2D}$ , Sedov's (1973) cylindrical blast-wave theory predicts

$$p_w(t) = P_{w(\tau_p \leq \tau_{2D})} \left( \tau_{2D} / t \right)^{\frac{1}{3}} \quad (2.15)$$

Hence, the total impulse per unit area over the impulse surface, assuming  $\tau_0 \geq \tau_{2D}$  and  $\tau_p \leq \tau_{2D}$ , can now be calculated as

$$\begin{aligned} \frac{I}{A} &= p_w \tau_p + p_w \tau_p \int_{\tau_p}^{\tau_{2D}} t^{-\frac{2}{3}} dt + P_{w(\tau_p \leq \tau_{2D})} \tau_{2D} \int_{\tau_{2D}}^{\tau_0} t^{-1} dt \\ &= p_w \tau_p \left\{ 1 + 3 \left[ \left( \frac{p_w}{P_{w(\tau_p \leq \tau_{2D})}} \right)^{\frac{1}{2}} - 1 \right] + \left( \frac{p_w}{P_{w(\tau_p \leq \tau_{2D})}} \right)^{\frac{1}{2}} \ln \left( \frac{P_{w(\tau_p \leq \tau_{2D})}}{P_{\infty}} \right) \right\} \end{aligned} \quad (2.16)$$

A schematic of the model for surface pressure versus time is presented by Pirri (1973) and is reproduced below in **Figure 2.6**. When  $\tau_p < \tau_{2D}$ , the surface pressure is  $p_w$  until  $t = \tau_p$ , with the pressure decay following Sedov (1959) planar blast wave model until  $t = \tau_{2D}$ . For  $t > \tau_{2D}$ , the surface pressure decays with time following Sedov's cylindrical blast wave model. For long pulses where  $\tau_p \geq \tau_{2D}$ , the surface pressure is  $p_w$  until  $t = \tau_{2D}$ , following the cylindrical decay model afterwards.

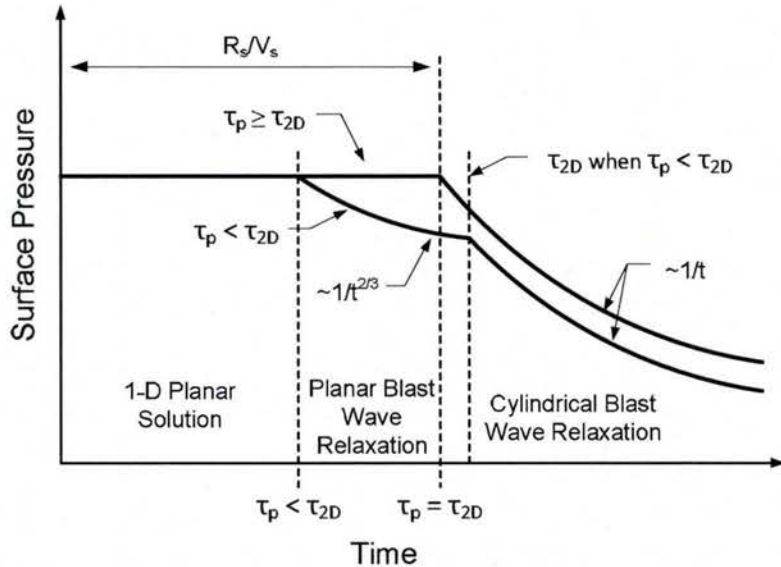


**Figure 2.6: Surface pressure vs. time evolution, showing characteristic times. (Pirri, 1973)**

A calculation was also performed for the impulse and coupling coefficient for the case of a finite diameter target surface. With a finite target, the blast wave pressure is not relaxed to atmospheric before “spilling” around the target’s periphery. Here a new characteristic time is introduced:  $\tau_D$ , which is the time taken by the cylindrical blast to reach the edges of the target—given by

$$\tau_D = \tau_{2D} \left( \frac{r_t}{r_s} \right)^2 \quad (2.17)$$

With  $r_t$  and  $r_s$  being the radius of the target and the radius of the laser spot, respectively. When  $t > \tau_D$ , the initial force is no longer preserved, due to the decaying pressure across the finite (constant) target area. Hence, the total impulse for a finite target size when  $\tau_p \leq \tau_{2D}$  and  $\tau_0 > \tau_D$ , is then given by

$$\begin{aligned}
I_{total} &= A_s \int_0^{\tau_{2D}} p_s(t) dt + \int_{\tau_{2D}}^{\tau_D} \int_0^{r_{bw}} p_s(t) (2\pi r) dr dt + A_T \int_{\tau_D}^{\tau_0} p_s(t) dt \\
&= A_s p_w \tau_p \left\{ 1 + 3 \left[ \left( \frac{p_w}{P_w(\tau_p \leq \tau_{2D})} \right)^{\frac{1}{2}} - 1 \right] \right\} + P_w(\tau_p \leq \tau_{2D}) A_s \left[ \tau_{2D} - \tau_{2D} + \frac{A_T}{A_s} \tau_{2D} \ln \left( \frac{\tau_0}{\tau_D} \right) \right] \quad (2.18)
\end{aligned}$$

with  $r_{bw}$  as the radius of the cylindrical blast wave, and  $A_s$  and  $A_T$  being the laser spot area and target area, respectively. The momentum coupling coefficient can then be calculated from  $C_m = I_{total}/E_p$ , in which the laser pulse energy is  $E_p = A_s I_0 \tau_p$ .

Slightly different results are obtained by **Richard (1989)**, where cylindrical blast wave relations were used to calculate the impulse on a horizontal line focus case, as described earlier. The equation describing the total impulse in this particular situation being

$$I_{total} = A_s p_s \tau_{2D} \left\{ 1 + 2 \left[ \left( \frac{p_s}{P_\infty} \right)^{\frac{1}{2}} - 1 \right] - 2 \left( \frac{p_s}{P_\infty} \right)^{\frac{1}{2}} - \left( \frac{P_\infty}{p_s} \right) \right\} \quad (2.19)$$

These analytical formulations will be applied next in analyzing experimental pressure transducer data obtained from the present test campaign.

### 3. Experimental Apparatus and Procedure

The LP experimental setup involved a Hypersonic Shock Tunnel (HST), one CO<sub>2</sub> laser, a 2-D cross-sectional LightCraft model, and requisite instrumentation/data acquisition system. Accurate triggering of all events was mandatory since the entire HST test window was typically ~3.0 ms depending on the desired HST flow condition, whereas the laser energy deposition time (~1  $\mu$ s) and subsequent blast wave expansion (~200  $\mu$ s) were substantially shorter. A more detailed description of the experimental setup is given below.

#### 3.1 Hypersonic Shock Tunnel

This experimental research was carried out at the Henry T. Nagamatsu Laboratory for Aerothermodynamics and Hypersonic (HTN - LAH) in Sao Jose dos Campos, Brazil, using the T3 HST facility to drive hypersonic flow over a 2-D LightCraft model for pulsed laser scramjet tests. The physics of shock tunnels is comprehensively covered in several references such as **Liepmann & Roshko (1964)**, **Lukasiewicz (1973)**, **Anderson (1990)**, and **Nascimento (1997)**, and won't be addressed further here except for a general technical description of the T3 facility. A more thorough introduction to Hypersonic Shock Tunnels is given in **Appendix C**, which includes the theory and modeling of impulsive HST flows. **Figure 3.1** shows the T3 hypersonic tunnel in the HTN-LAH laboratory.

The T3 tunnel enables test section flow conditions varying from low to high enthalpies, simulating Mach numbers from approximately 6 up to 15, by replacing the nozzle throat and exit sections and varying the driver section pressure and gas composition (i.e., dry air for low enthalpy runs, and helium for higher enthalpies). For this particular HST, test times vary from 2 to 10 ms, with longer test times for lower Mach numbers. The tunnel can generate flows with enthalpies up to 10 MJ/kg, with reservoir pressures up to 25 MPa, which leads to stagnation pressures up to 200 atm and stagnation temperatures up to 7500 K in the test section.



**Figure 3.1: T3 Hypersonic Shock Tunnel at the HTN-Laboratory of Aerothermodynamics and Hypersonics.**

This tunnel is composed of a 4.08 m long driver section that can operate at pressures up to 35 MPa (5000 psi, 345 bar), even though in the present experiment most test runs were performed with 3000 psi of filling pressure. A double diaphragm section (DDS) is placed between the driver and driven sections. The DDS houses four solenoid valves and the stainless steel diaphragms that control the exact moment of the experiment initiation; a third diaphragm can be used to operate the tunnel in the Gaseous Piston mode if required (Nascimento, 1997). This DDS section is usually filled at half of the driver's pressure and once this section is rapidly vented by activating the solenoid valves, the higher differential pressure forces the rupture of both diaphragms and hence, the onset of HST operation. Argon was selected for DDS working fluid since it is an inert gas with high molecular weight, which helps to prevent gas diffusion between the (Helium/Air) contact surface formed after the diaphragms burst.

A contraction region is placed just downstream of the DDS which reduces the diameter of the driver section to match that of the driven, reduced from 190.5 mm to 127

mm; this produces a stronger shock wave than the same driver-to-driven pressure ratio could produce in a comparable, constant-area shock tube.

The driven section is 10.5 m long with 127 mm internal diameter, and its downstream nozzle-end is strengthened to serve as a “reservoir” for the high pressure reflected region, when operated in the reflected mode. Instrumentation ports are distributed along the entire length of the tunnel to accommodate all diagnostics required for a given experiment. In the present work, this section was fitted with three pressure transducers, two of which were separated 400 mm apart and used to measure the incoming shock wave speed. The third pressure transducer, installed at the end section close to the diverging nozzle entrance, was used to measure the reservoir pressure as well as to trigger the remaining test equipment, including the Cordin high speed digital camera, the Lumonics 622 CO<sub>2</sub> laser, and the data acquisition system. Installed at the downstream end of the driven section is an aluminum diaphragm that separates this section from the evacuated dump tank. Upon the arrival of the incident shock wave, this diaphragm breaks from the sudden pressure increase, and releases the shock-compressed test gas into the nozzle section.

The convergent-divergent nozzle section comprises a replaceable “throat” insert and 15° half-angle, multi-section conical nozzle. For most experiments performed in the present research, the last nozzle section was removed to decrease the standard 610 mm exit diameter (which gives an ideal Mach number of 10.0), down to 491.0 mm for an ideal Mach number of 9.12. The nozzle resides inside an evacuated, two-segment dump tank; the hypersonic flow exits into a horizontal 1.8 m diameter by 1.26 m long segment (containing the test section), joined to a vertical segment measuring 1.89 m diameter by 4.35 m tall. The test section is fitted with a horizontal hollow sting mount (designed to support test models) that also provides a 20 cm (clear-aperture) beam tube for laser beam injection. An anodized aluminum infra-red (IR) window mount had to be designed, constructed, and installed onto the external end of this hollow sting (see **Figure 3.2**), and fitted with a 2 inch thick NaCl window.



**Figure 3.2: Hollow HST sting with IR window and mount installed.**

The test section/dump tank is equipped with four orthogonally-placed ports with 50 cm aperture for optical diagnosis (e.g., Schlieren visualization) and instrumentation feed-throughs. The top and bottom ports are strong enough to support heavy models, as in the current research, and also provide electrical feed-throughs for instrumentation such as pressure and heat transfer gages. In the present experiments the test section side ports were fitted with 30 cm quartz windows for maximum quality Schlieren photographs.

The T3 tunnel was a recent acquisition of the HTN-LAH so a few operational issues were still being addressed, and had to be tackled during the present campaign. One such issue was the lack of HST nozzle inserts that could permit operation at Mach numbers other than 10; this was resolved by the design and machining of five new stainless steel throat inserts for nominal Mach numbers of 6, 7, 8, 12, and 15.

Two new batches of stainless steel plates of the proper thickness were acquired for DDS diaphragm manufacture, with slightly different material compositions and thus different rupture dynamics. DDS diaphragms must be cross-cut machined (i.e., crucifix pattern) into the downstream-facing surface to enable them to burst open in the desired manner, with the creation of four petals (see **Figure 3.3**, central image). An incorrect cut depth (i.e., too deep) might lead to petal detachment and acceleration downstream through the driven tube, with fragments passing through the small HST nozzle throat and

impacting the model at ballistic speeds, often causing severe damage. Several test runs were performed with the two families of diaphragms until the right cut depth was found, as will be explained later. Furthermore, to reduce the risk of detached diaphragm petals damage, a “petal catcher” was designed and manufactured, as shown in **Figure 3.3** (left); at the far right is a pre-scored diaphragm, along with a burst diaphragm (center).



**Figure 3.3:** ‘Petal catcher’ (left), and stainless steel diaphragms (right).

The turnaround time for the experiments performed at the T3 facility is approximately 6 hours, including: a) replacement of used diaphragms at DDS and nozzle sections, b) purge of the residual gases, c) refill of driver and driven sections with new ‘gas loads’, and d) vacuum purge of the test section dump tank. Future improvements to this facility will greatly reduce this turnaround time, allowing multiple experiments in a single day.

### 3.2 Lumonics TEA-620 Laser and Beam Propagation

Pulsed infrared laser energy was supplied by one of the two Lumonics TEA-620 CO<sub>2</sub> lasers available, which share the same resonator cavity. An attractive feature of these TEA-620 lasers is their ability to deliver a very short (~1  $\mu$ s), high energy pulse, up to 500 J each, while operating in the stable resonator mode with peak powers of 2.2 GW, according to the manufacturer. In the unstable resonator mode used throughout this work, the TEA-620 has a small output beam divergence measured in the sub-miliradian

range, with pulses up to 300 J. Concerns about the limited lifespan of the high voltage capacitors (8 per laser), and the potential damaging effects of supply-side over-voltage oscillations—all led to conservative decision to operate the 620s at 65 to 70 % of their rated maximum capacitor charge of 100 kV; higher supply voltages produced frequent electric arcs, and lower voltages, inconsistent glow discharges. This decision reduced the 620's available output laser energy to approximately 150 to 230 J/pulse, but greatly increased reliability.

Note that both 620 lasers are now “on line” and they can be fired sequentially for multi-pulse LP experiments to examine the interaction of two laser-induced blast wave within a laser scramjet engine, under simulated ultra-high PRF conditions (e.g., 10 to 20 kHz). However, throughout the present campaign technical issues with one capacitor bank put it out of commission. Future experiments will be able to take advantage of the two lasers operating together. **Table 1** shows the basic operating conditions for each TEA-620 operating as a standalone unit, assuming 90kV for the charging voltage.

**Table 3.1: Basic operating conditions of Lumonics TEA 620 laser (stable resonator mode).**

Electrode Gap	200	mm	Capacitor	0.15	$\mu$ F ea.
Electrode length	600	mm	# Caps	2	/ stage
Charging Voltage	90	kV	# Stages	4	/ Marx
Electrical Energy	4860	J	Total C	0.075	$\mu$ F
Rep rate	0.03	Hz	Power input	145.8	W
Discharge volume	24	liters	FWHM	~100	ns
Energy density (input)	202.5	J/l			
Electric Field	18	kV/cm			
Output Energy(Photons)	500	Joules			
Electrical Efficiency	0.1029				

Lumonics TEA 620 lasers can operate with several different gas mixtures that produce different laser output pulse profiles and energies. The lasers currently operate in a “flow-through,” open-cycle mode wherein the gas mixture is controlled by varying the flow rate of each gas constituent; in the future, the system will likely be converted to closed-cycle operation, aided by an existing catalytic converter. Throughout the present test campaign a high gain (HG) mixture was used, which produced a short ~1  $\mu$ s pulse with a higher fraction of the pulse energy contained in the initial ~90 ns spike than in the

long tail. The laser pulse characteristics achieved with this HG mixture are displayed in **Table 3.2**.

The physics and operating principles for TEA CO<sub>2</sub> lasers can be found in several useful references (**Patel, 1968; Siegman, 1986; Svelto, 1998 and Verdeyen, 1994**), and need not be addressed further here.

**Table 3.2: Lumonics TEA-620 laser pulse characteristics with high gain gas mixture.**

<i>Parameter (units)</i>	<i>Value</i>
Energy per pulse, J	150-230
Wavelength, $\mu\text{m}$	10.6
Peak pulse duration (FWHM), ns	90-100
Maximum peak power, MW	~1800
Total pulse duration, $\mu\text{s}$	~1.0
HG gas mixture flow, $\text{ft}^3/\text{hr}$	16.0 He; 6.5 CO <sub>2</sub> ; 3.2 N <sub>2</sub>
Power supply voltage, kV	65-70

These TEA lasers were shipped from the United States to the HTN-LAH laboratory in Brazil in dire condition, basically having been ‘mothballed’ since mid- 1980s being last used as amplifiers in the “Paladin” seed laser that fed the Induction-LINAC Free Electron Laser (FEL) experiment at Lawrence Livermore National Laboratory (LLNL). Hence, for the present campaign, the laser optics had to be designed for the 622-TEA unstable resonator configuration, wherein the same resonator cavity shared by both 620 modules. An *unstable* resonator was selected over the *stable* resonator configuration for one principal reason: i.e., the elevated mezzanine planned for the 622 installation placed them at a distance of ~25 meters from the HST test section, which demanded the lower divergence beam from an unstable resonator, even though the output pulse energies were lower (e.g., 320J vs. 500J from each 620 module).

The unstable resonator optics for the 622 configuration (see **Figure 3.4**) are comprised of a large concave parabolic mirror (the primary reflector) and a smaller convex parabolic mirror or output-coupler, separated by 3.75 m length; the cavity encompasses both 620 modules that are precisely positioned, in line, upon two steel rails. The aluminum primary reflector is 254 mm (10”) in diameter and 50.8 mm thick,

diamond turned to a concave geometry with 15 m surface radius. The output coupler is a 120 mm diameter aluminum mirror with truncated sides and 100 mm in width, diamond turned to a 7.5 m convex surface radius. Thus, these mirrors form a resonating cavity with a magnification of 2, giving a collimated output beam, as shown in **Figure 3.5**.

Sturdy welded steel support stands were fabricated for the resonator optics, and anchored firmly into the mezzanine's reinforced concrete floor (see **Figure 3.5**). These detached optic stands neatly isolated the resonator optics from shock-wave-induced vibrations from 620 laser firings that could misalign the output optics, if they had been attached directly to the laser modules and/or their support rails. This was of extreme importance since precise alignment of the unstable resonator optics is a labor intensive, time consuming process. Finally, note in **Figure 3.5** (left) that the 622 system is completely enclosed by a Faraday cage which attempted to provide an EM leak-proof envelope; displayed at the right is a typical laser beam footprint "burned" onto ThermoFax paper.

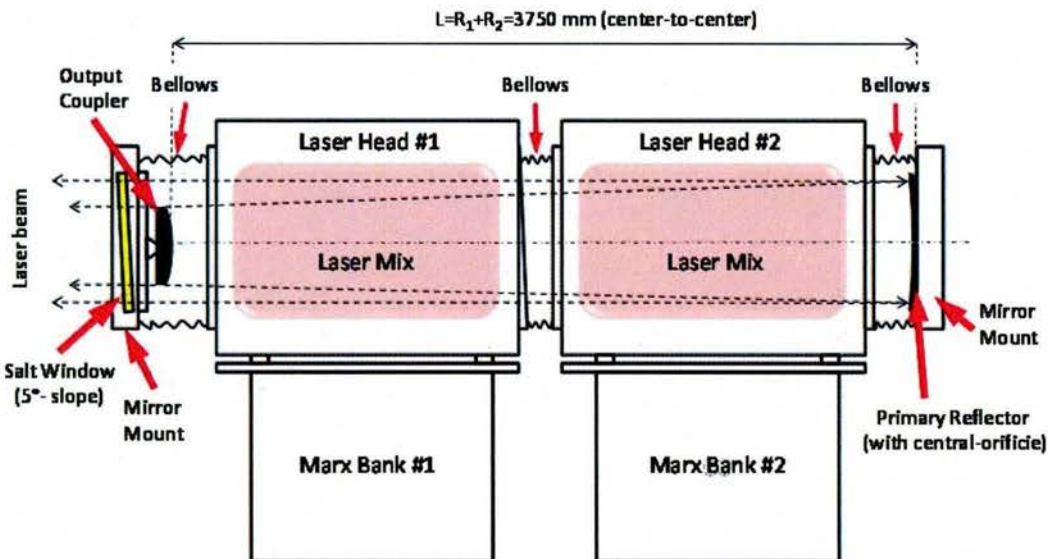


**Figure 3.4: TEA 620 Laser configuration with unstable resonator cavity.**

In addition to the laser resonator optics, other critical parts had to be designed, constructed, and/or acquired in order to reactivate the laser. One of these was the NaCl laser output window (transparent to 10.6  $\mu\text{m}$  infrared radiation, and installed into the output coupler framework) to seal off the internal laser gas mixture from infiltration and

contamination by the surrounding atmosphere. To complete the cavity isolation from the lab environment, three rubber bellows were installed: one between the two laser modules, another at the rear primary mirror, and another to seal off the output window.

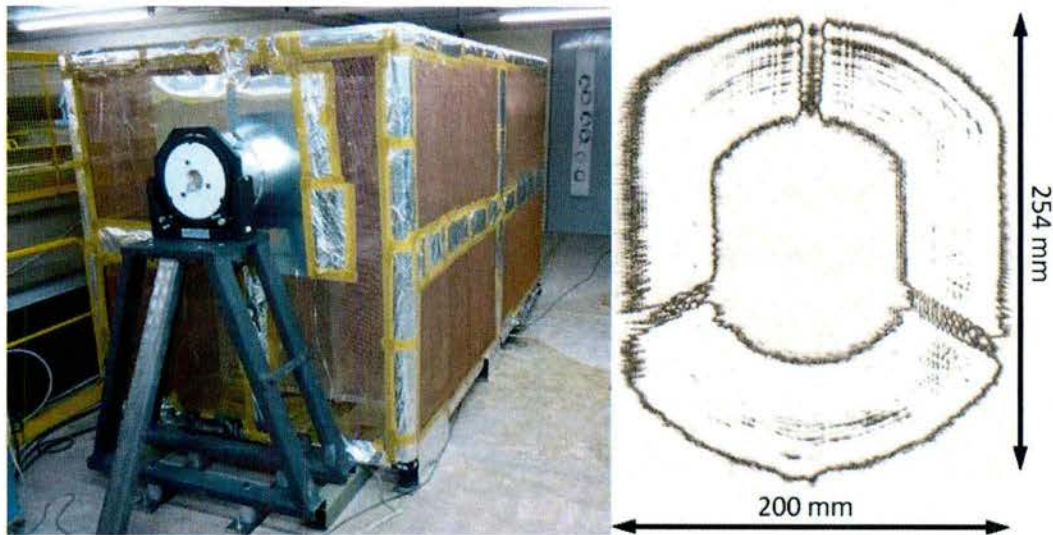


**Figure 3.5: TEA 622 laser system with Faraday cage (left), and beam footprint (right).**

Due to limited space available in the HTN-LAH laboratory, an adjacent elevated mezzanine was acquired for installation of the 622-TEA laser system, as mentioned earlier. Since this mezzanine was ~25 meters from the HST sting-entry window, a special “light-tight” laser beam delivery tube (made from 350 mm diameter PVC pipe) had to be erected to safely transmit laser power into the HST test section. Also, the three 45-deg. turning points in this beam tube, required 30cm diameter turning flats—additional metal mirrors that had to be designed and manufactured, and then bolted to adjustable mirror mounts.

As shown in Figure 3.6 the laser beam delivery path, starting at the 622 laser, encounters a sequence of optical elements (i.e., the “optical train”) which are arranged in the following order: First, the beam leaves the 622-TEA output coupler with a diameter of 254 mm (10 in) and arrives at the 0.75x magnification (reducing) telescope. This telescope was designed around a pre-existing 300 mm (12 in.) diameter concave copper mirror with surface radius of 10 m, and hence required the fabrication of one additional convex metal mirror. After reflecting off the concave mirror, the incident beam strikes a 228.6 mm (9 in) diameter convex aluminum mirror placed 1.25 m away, requiring a

mirror curvature of 7.5 m to regain beam collimation. This reduced aperture beam fit nicely through the three 300 mm diameter turning mirrors (placed at 45 degrees to the incident beam at the corners of the beam delivery tube in **Figure 3.6**), as well as clearing the 200 mm aperture window installed with a 7 deg. incidence at the HST hollow sting (see **Figure 3.2**).

After the reducing telescope is properly aligned to “burn” a centered ThermoFax pattern at the first turning flat, all three 300 mm flats (two aluminum and one copper) must then be precisely adjusted (in sequence, again by burning thermally sensitive paper) to deliver a centered “burn” at the HST sting-mount window. This 250 mm diameter, 50 mm thick NaCl window serves a dual purpose: 1) a physical boundary to isolate the high vacuum dump tank volume (necessary for the HST operation) from the lab environment; and, 2) a beam splitter that diverts a small portion of laser pulse energy into a calorimeter (*joule meter*)—a sensitive diagnostic unit used to precisely measure and record the delivered laser pulse energy—as well as a photon drag detector to measure the pulse profile, at every shot. This arrangement is depicted in **Figure 3.6**.

The NaCl windows reflect approximately 8% of the incident 10.6  $\mu$ m beam energy, which is diverted onto a concave copper mirror of 250 mm diameter and 2 m surface radius, which concentrates the focused beam through a second NaCl window and onto a Gentec UP60N-40S-H9 thermopile calorimeter. This second oblique NaCl window (labeled #2 in Figure 3.7) diverts ~0.64% of the laser energy into a Hamamatsu B749 photon drag detector, for the measurement of the pulse profile.

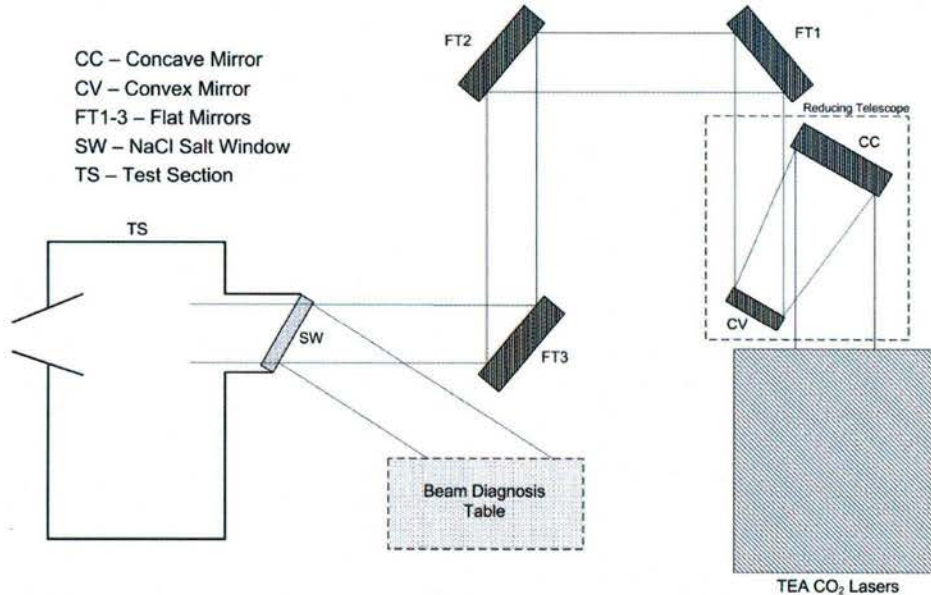


Figure 3.6: Laser beam transmission path through the laboratory to the test section.

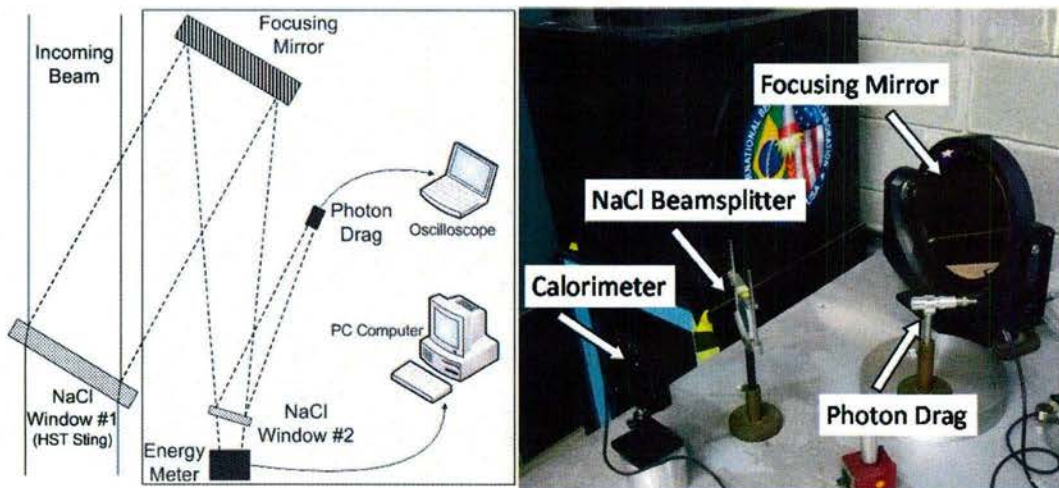
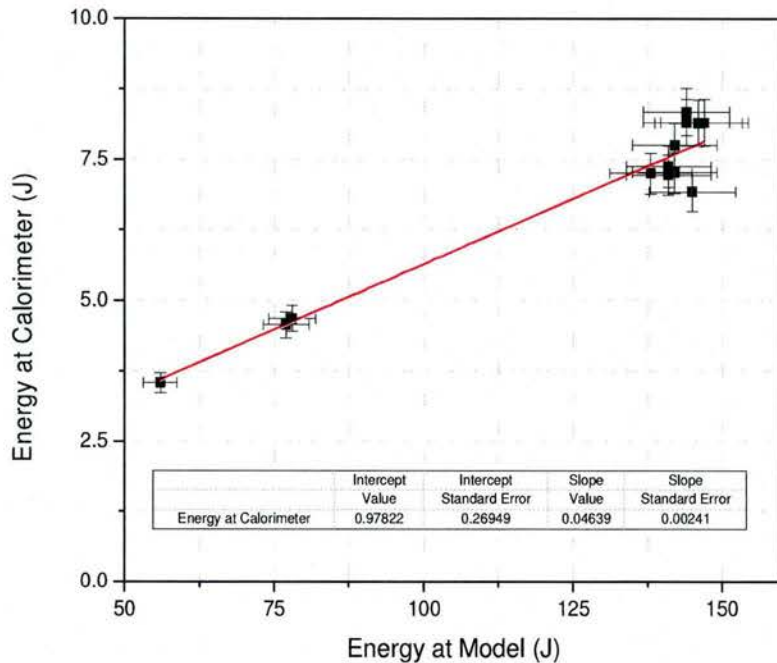


Figure 3.7: Beam diagnostics table for analyzing laser beam energy and pulse profile.

### 3.2.1 Laser Beam Diagnostics and Calibration

As indicated above, a beam diagnostics table was set up for measuring laser pulse energy for every test run. The following describes the calibration procedure. First, the large NaCl window/beam-splitter (see **Figure 3.2**) had to be calibrated, which required two calorimeters: 1) one placed inside the HST test section, just downstream of the 2D Lightcraft model (Scientech Astral Series S, 200 mm aperture) to capture the actual energy incident onto the test model, and, 2) a second calorimeter placed outside, near the

sting, to collect the reflected portion of the beam (Gentech UP60N-40S-H9) entering the sting window. The NaCl windows supplier specified a reflectivity of 7.5%, but the actual reflectivity was measured at 7.9%. The beam-splitter calibration plot is given in **Figure 3.8**, together with the linear fit results and corresponding instrument measurement error.



**Figure 3.8: Beam-splitter energy calibration curve for NaCl sting-window.**

The laser pulse profile (or time-history of irradiance) was obtained with the use of a secondary beam-splitter and a photon drag detector as mentioned above (see **Figure 3.7**). This pulse profile was obtained/ recorded at every laser shot, and is dictated by the laser kinetics for the gas composition filling the active cavity volume. It is also dependent on the final Marx bank voltage, available energy, and discharge dynamics; the Hyptronics power supply was set to either 65 kV or 70 kV for the charge.

The energy profiles sampled throughout this experimental campaign revealed little variation, because the laser gas mixture composition was kept unchanged. The pulse profile in **Figure 3.9** below indicates that approximately 70% of the pulse energy resides in the spike, with the remaining 30% in the  $1.5\mu\text{s}$  pulse tail.

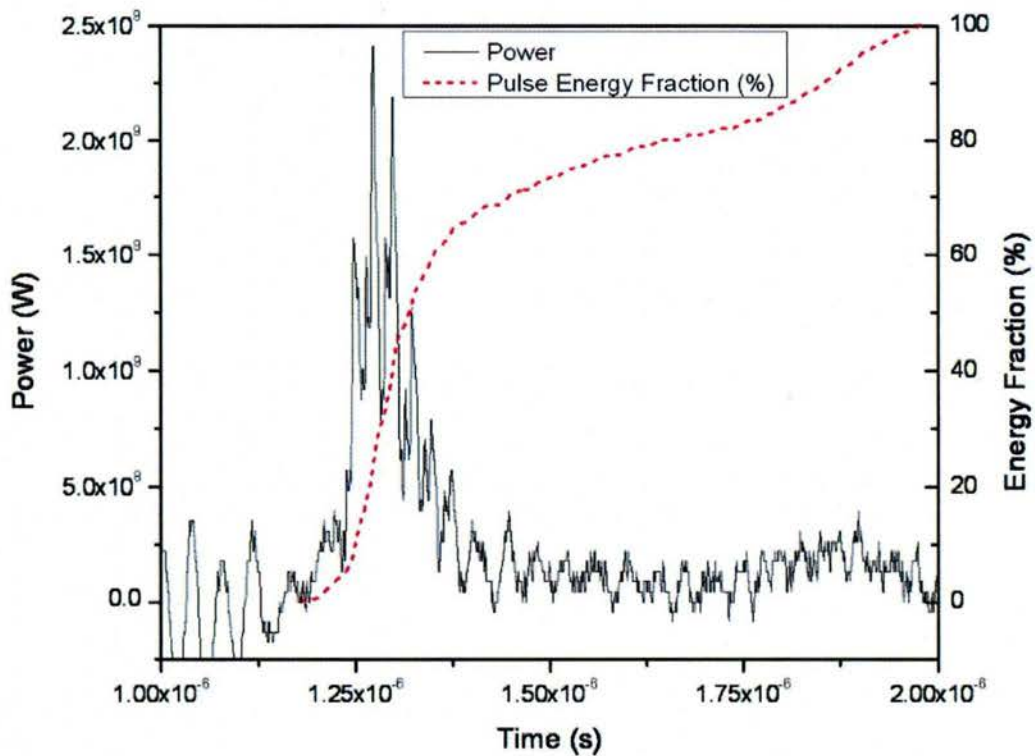
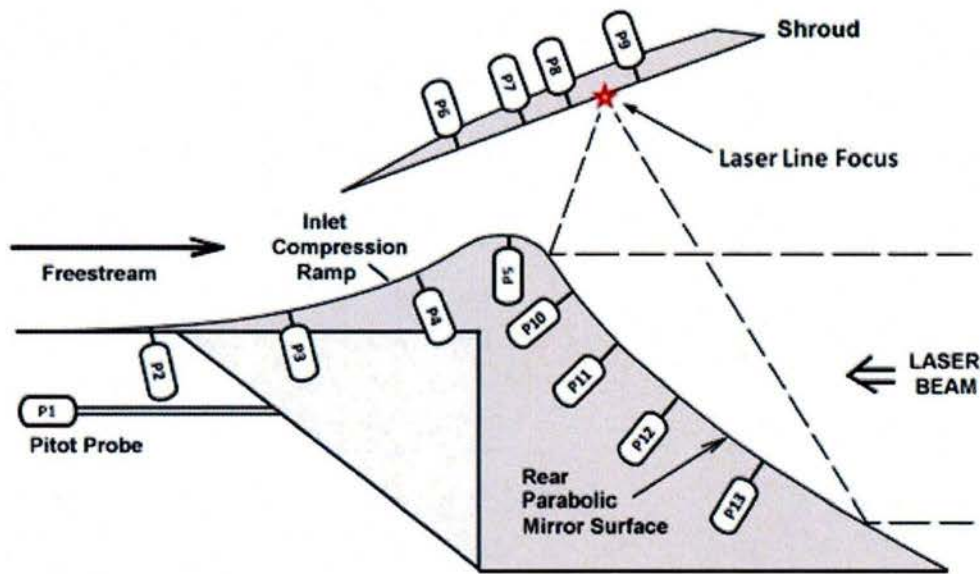


Figure 3.9: Laser pulse profile and integrated pulse energy sampled at NaCl sting-window.

### 3.3 2-D Cross Section Lightcraft Model

This 2-D airbreathing engine model is approximately a half-scale representation of a 1/24<sup>th</sup> annular section of the 1.4 m diameter LightCraft Technology Demonstrator (LTD) analyzed by **Myrabo (1989)** and **Richard (1989)** for the now-defunct SDIO Laser Propulsion Program, and is scaled to fit inside the HST 0.6 m T3 test section. A derivative of previous LP research performed at RPI, the 250 mm wide, 2-D aluminum model is comprised of three basic parts: i) forebody compression ramp; ii) inlet/shroud; and, iii) primary parabolic mirror/expansion surface. The external compression inlet forebody directs the captured airflow, across the shroud's flat plate (lower) impulse surface that bounds the laser absorption chamber. When the incoming laser beam is brought to a line focus (as shown in **Figure 3.10**) upon this shroud undersurface, the aluminum "igniter" material greatly lowers the incident laser intensity and fluence required to trigger the optical air breakdown, as explained in **Chapter 2**.

The geometry for this model's external compression air inlet is similar to that studied by **Richard (1989)** and reminiscent of the work performed by **Sienel (1992)**, but the length was truncated to represent only part of an actual scale nosecone in order to fit within the T3 HST nozzle. **Figure 3.10** depicts the 2-D model contour together with the position of the pressure sensors. The compression ramp section is instrumented with 3 pressure transducers ( $P_2$ ,  $P_3$ , and  $P_4$ ) distributed lengthwise along the centerline.



**Figure 3.10: Pressure sensor positions within 2D model geometry.**

Following the compression ramp, comes a smooth transition or “throat” section (fitted with  $P_5$  in **Figure 3.10**) just upstream of the primary focusing optics. This rear parabolic reflector has three main functions: 1) focus the incoming laser beam to cause the electrical air breakdown on the shroud undersurface; 2) act as an inner lower boundary of the absorption chamber, containing the subsequent cylindrical blast wave generated by laser induced breakdown; and, 3) participate as an expansion (2D plug nozzle) surface for the blast-wave-processed engine working airflow. In this 2-D model the primary reflector is composed of a sturdy aluminum “hardback” machined with the desired parabolic contour, to which a polished OFHC copper faceplate was attached to create the 2-D mirror; this optic was designed for unrealized LP experiments proposed by **Fernandez (1990)** and by **Sienel (1992)**. The primary rear reflector was fitted with four pressure sensors ( $P_{10}$  thru  $P_{13}$  in **Figure 3.10**).

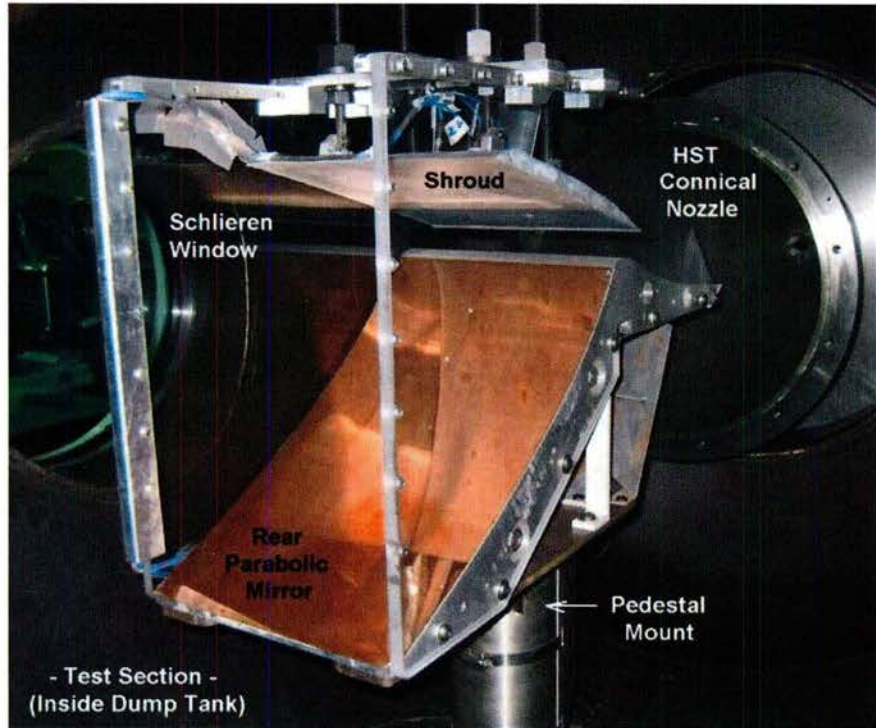


**Figure 3.11: 2-D laser propulsion model installed in T3 hypersonic shock tunnel.**

The 2-D shroud provides both air inlet capture and absorption chamber functions, and its shape is similar to that adopted by Katsurayama (2001-2004) in his  $M=5.0$  numerical analysis, as well as the LTD's shroud contour used in the previous conceptual studies. The 2-D shroud is comprised of a simple planar inner wall, with a streamlined cylindrical exterior surface that is of lesser importance in the current experiments; the shroud was also fitted with four pressure transducers ( $P_6$  thru  $P_9$  in **Figure 3.10**). **Figure 3.11** shows the model installed in the HST test section.

Because of the varied test conditions that can be simulated in the HST, the 2-D laser scramjet model was designed in a modular manner so that most parts can be exchanged with the current configuration—considered the first in a series of Lightcraft engines to be tested in the near future. The shroud can be placed at different positions with respect to the model's center-body (i.e., compression ramp + primary reflector), since the mechanical support system for the articulating shroud was designed for three degrees of freedom: 1) fore and aft translation; 2) up and down translation; and, 3) free rotation for changing angle-of-attack. For the static (i.e., quiescent flow) experiments performed in this work, the laser line focus was kept at the same axial position upon the shroud

undersurface as shown in **Figure 3.12**; to change angle-of-attack for the static and initial hypersonic experiments, the shroud is simply rotated about this line focus. **Table 3.11** shows the radial distance of the sensors to the laser line focus for the initial axial shroud position. During the hypersonic experiments, the axial focal line position was varied across the shroud to accommodate desired test conditions.

**Table 3.3: Pressure sensor inventory and radial distance from laser focal line at the shroud's undersurface.**

<i>Sensor</i>	<i>Radial distance from focus[mm]</i>	<i>Sensor</i>	<i>Radial distance from focus[mm]</i>
1	Pitot	8	25
2	294	9	25
3	234	10	130
4	175	11	160
5	116	12	200
6	125	13	260
7	55	-	-

The influence of the radially expanding flow field exiting the HST conical nozzle was neglected in the present experiments; the hypersonic flow is “channelized” to some extent by the 2-D model’s polycarbonate side panels. The principal function of the side panels was to support the shroud while providing an unobstructed view of the laser-induced gasdynamic phenomena taking place within the absorption chamber. These side panels introduce oblique shock waves into the engine interior flow field, phenomena which was deliberately not visualized (i.e., purposefully avoided) in the Schlieren setup. Future detailed investigations of such shock-induced perturbations, as well as more detailed analyses of the external compression inlet characteristics, must await further instrumentation and testing. Nevertheless, to accomplish the principal research objectives of the present campaign (i.e., first-order analysis of impulse generation physics, and overall process efficiency), these interference/ perturbation effects can be neglected.

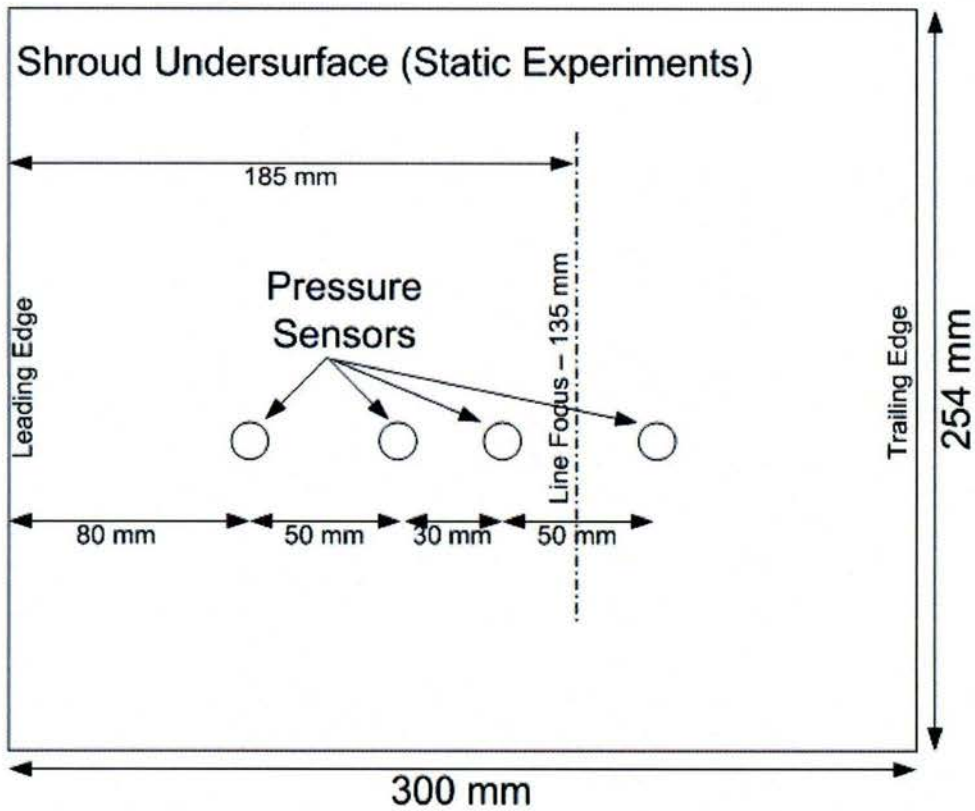


Figure 3.12: Sensor disposition on shroud undersurface and line focus position used during the static experiments.

### 3.4 General Instrumentation

A full diagnostic array is required to monitor all essential components of the experimental setup which includes the T3 tunnel, 622 laser system, and experimental model. The T3 shock tunnel is instrumented with three piezoelectric pressure transducers: two Kistler Model 701A gages for measuring the incoming shock wave speed in the driven section, and one Kistler 701K for the sensing reservoir pressure—needed to calculate T3 test section flow conditions upon the model. The initial pressure (i.e., prior to HST “firing”) inside the evacuated dump tank and test section is measured by a BOC Edwards APG-L-NW16 Active Pirani vacuum gauge, read by a Model 1575 pressure display. All remaining critical HST pressures (e.g., driver, DDS, etc.) are measured by analog Heise mechanical/analog gauges installed into the T3 control panel. Finally, a Schlieren visualization setup with high speed digital Cordin camera captures the hypersonic flow structure through the T3 test section, for subsequent analysis.

The TEA-620 laser system is fitted with a Teledyne Model 3190 trace oxygen analyzer for measuring O<sub>2</sub> contamination levels in the laser gas mix, to assure that a “glow discharge” is established across the resonator electrodes instead of damaging arcs; note that O<sub>2</sub> concentrations of 500 ppm and higher can encourage electrical arcs during laser firings. These arcs prevent the uniform, ‘glow’ discharge required for an effective lasing of the active media (CO<sub>2</sub>) greatly reducing the energy output and also inducing strain in the system, what reduces its lifespan. As mentioned before, the incoming laser pulse energy from the TEA-620’s is measured by two thermopile calorimeters: Gentec UP60N-40S-H9, and Scientec Astral 360801S. Both TEA-620 lasers are controlled by a single customized control panel, with separate controls for the 100 kV Hyptronics power supply that charges the Marx banks.

The 2-D model was instrumented with thirteen piezoelectric PCB pressure transducers: twelve for measuring the pressure distribution vs. time along the model centerline, and one installed in a separate pitot probe for sensing the stagnation impact pressure of incoming hypersonic flow, as mentioned in the previous section.

The 2-D laser scramjet model was also fitted with four Nanmac Type K surface junction thermocouples (Model E6-Q7982-2): two located upon the shroud inner surface and two in the primary reflector, to record the time-variant surface temperatures from which local heat transfer rates were to be obtained using the Cook-Felderman technique (**Cook and Felderman, 1966**). As later revealed in tests, these sensors proved to lack the desired sensitivity for single-pulse LP experiments. More sensitive sensors, as used by **Salvador (2005, 2007)** will have to be used in future multi-pulse experiments, in an attempt to directly measuring the global heat transfer onto interior engine surfaces.

### 3.5 Schlieren Visualization Setup

An ultra-high speed Cordin digital movie camera was implemented with a Schlieren optical visualization setup for analyzing the time-dependent flow-field structure inside the 2D laser scramjet engine; the objective was to capture the evolving LSD wave driven, expanding blast wave dynamics, and subsequent unpowered blast/flow interactions within the engine working fluid. This visualization system uniquely provides the ability to observe density variations in the flow during pulsed operation of the

Lightcraft engine. More details on the design and setup of Schlieren systems and associated theory is given by **Settles (2006)**, and will not be further addressed here.

The mirror-based Schlieren setup adopted a standard 'Z' configuration with two flat folding mirrors with the test section in between. A schematic of this system is depicted in **Figure 3.13**. The effective viewing aperture 250 mm in diameter, dictated by the size of the quartz windows installed in the two test section ports bounding the test section. This Schlieren system is composed of a pulsed xenon flash lamp, an optical slit and focusing lens, two parabolic and three flat mirrors, the knife edge which provides the necessary light cut-off, and the Cordin 550 rotating mirror, ultra-high speed camera. The photo in **Figure 3.14** shows the Schlieren light beam path and placement of the Cordin camera, with respect to the T3 test section.

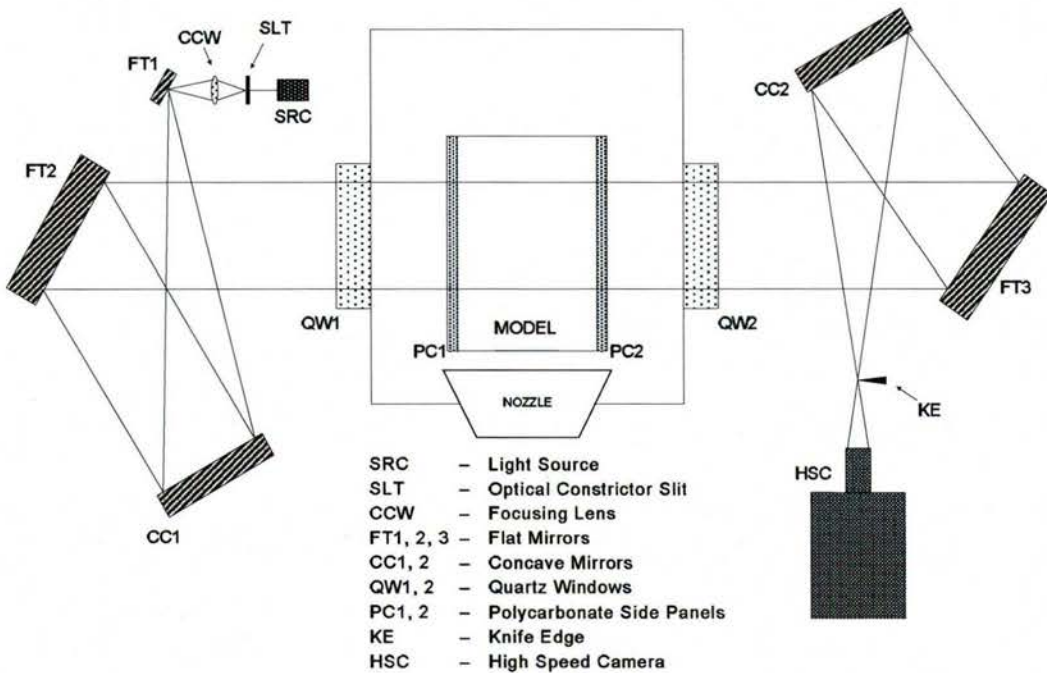


**Figure 3.13: Schlieren visualization and Cordin camera system setup for T3 test section.**

The Cordin 550 camera can acquire 32 frames with a maximum resolution of 1000 x 1000 pixels at up to 2 million frames per second (fps) in full color. Such frame rates are achieved by a multi-faceted mirror spinning at high speeds, surrounded by 32 CCD elements which acquire images as the mirror rotates. Mirror rotation is driven by a turbine wheel supplied with high pressure N<sub>2</sub> for frame rates up to 500,000 fps, and pressurized He for the highest speeds. Even though extremely high speeds can be

achieved, the present work demanded more modest 50,000 to 100,000 fps because of technical reasons related to the high Electro-Magnetic Interference (EMI) generated when the 620-TEA lasers were fired. This EMI impaired the Cordin's ability to acquire uninterrupted image sequences, as well as the loss of triggering precision which must be on the order of microseconds to capture the desired "window" that images the laser breakdown and subsequent flow field evolution. Hence, the requirement for lower frame rates and the implementation of a specific, known camera pre-trigger to insure capture of the desired "test window." Since triggering precision is closely tied to frame rate, attempts to run the camera at the highest frame rates in that excessive EMI environment, has caused several HST runs to miss the intended "window" altogether—sometimes by a large margin.

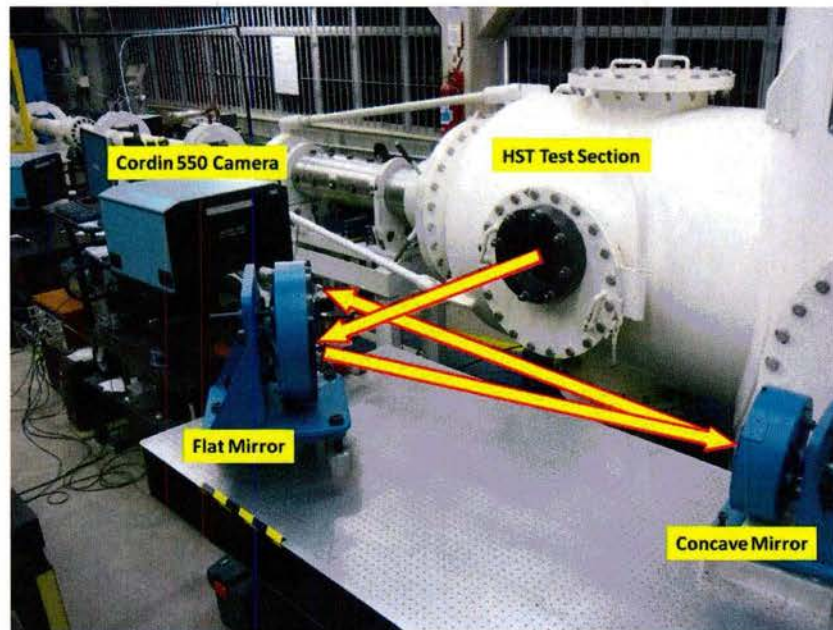


Figure 3.14: T3 Hypersonic Shock Tunnel showing Schlieren light path and Cordin 550 camera.

### 3.6 Data Acquisition

For the present laser scramjet experiments performed in the T3 tunnel, the data acquisition system required more than 18-20 channels, depending on the test objectives. For the 2-D Lightcraft model alone, 13 channels were needed for the piezo-electric pressure transducers, whereas the HST instrumentation required another set of 4 channels; additional channels were needed for TEA-620 laser diagnostics.

Two 16-channel Yokogawa DL750 Scopemeters comprised most of the data acquisition system: one for the LP model pressure distributions, and the other for HST instrumentation. These DL750s can record up to 10 MS/s for all 16 channels for the duration of the test window (e.g., 10 ms for the HST scope, and 5 ms for the 2-D model scope); that provides the required 10 sample points per microsecond of test time—judged sufficient to resolve all physical phenomena under investigation. Raw pressure data from the model's piezo-electrics was pre-amplified by a 16-Channel PCB 481A02 signal conditioner. The Yokogawa DL750 easily interfaced with the favored data analysis software (Microcal Origin), without the need for preprocessing.

Data acquisition for the TEA-620's diagnostic instrumentation was performed by a Tektronix TDS2014 (100 MHz, 1GS/s); the laser pulse profile was sensed by a Hamamatsu B749 Photon Drag detector. The Gentec's UP-60N calorimeter readout was acquired by a Pentium PC computer.

All remaining data gathered during the LP experiments (laser gas constituent feed rates, HST driver/driven pressures, etc) was hand recorded from direct readouts on standard analog gauges and other stand-alone instruments.